Meteoritics & Planetary Science 37, 371–394 (2002)
Available online at http://www.uark.edu/meteor

Northwest Africa 032: Product of lunar volcanism

T. J. FAGAN[1†*], G. J. TAYLOR[1], K. KEIL[1], T. E. BUNCH[2], J. H. WITTKE[3], R. L. KOROTEV[4], B. L. JOLLIFF[4], J. J. GILLIS[4], L. A. HASKIN[4], E. JAROSEWICH[5], R. N. CLAYTON[6], T. K. MAYEDA[6], V. A. FERNANDES[7], R. BURGESS[7], G. TURNER[7], O. EUGSTER[8] AND S. LORENZETTI[8]

[1]Hawai'i Institute of Geophysics and Planetology, School of Ocean and Earth Science and Technology, University of Hawai'i at Manoa, Honolulu, Hawai'i 96822, USA
[2]Space Sciences Division, NASA Ames Research Center, Moffett Field, California 94035, USA
[3]Department of Geology, Northern Arizona University, Flagstaff, Arizona 94035, USA
[4]Department of Earth and Planetary Sciences, Washington University, St. Louis, Missouri 63130, USA
[5]Department of Mineral Sciences, Smithsonian Institution, Washington, D.C. 20560, USA
[6]Enrico Fermi Institute, University of Chicago, Chicago, Illinois 60637, USA
[7]Department of Earth Sciences, University of Manchester, Manchester, M13 9PL, U.K.
[8]Physikalisches Institut, University of Bern, CH-3012 Bern, Switzerland
[†]Present address: Tokyo Institute of Technology, 2-12-1 Ookayama, Meguroku, Tokyo 152-8551, Japan
*Correspondence author's e-mail address: fagan@geo.titech.ac.jp

(Received 2001 May 8; accepted in revised form 2001 December 6)

Abstract–Mineralogy, major element compositions of minerals, and elemental and oxygen isotopic compositions of the whole rock attest to a lunar origin of the meteorite Northwest Africa (NWA) 032, an unbrecciated basalt found in October 1999. The rock consists predominantly of olivine, pyroxene and chromite phenocrysts, set in a crystalline groundmass of feldspar, pyroxene, ilmenite, troilite and trace metal. Whole-rock shock veins comprise a minor, but ubiquitous portion of the rock. Undulatory to mosaic extinction in olivine and pyroxene phenocrysts and micro-faults in groundmass and phenocrysts also are attributed to shock.

Several geochemical signatures taken together indicate unambiguously that NWA 032 originated from the Moon. The most diagnostic criteria include whole-rock oxygen isotopic composition and ratios of Fe/Mn in the whole rock, olivine, and pyroxene. A lunar origin is documented further by the presence of Fe-metal, troilite, and ilmenite; zoning to extremely Fe-rich compositions in pyroxene; the ferrous oxidation state of all Fe in pyroxene; and the rare earth element (REE) pattern with a well-defined negative europium anomaly. This rock is similar in major element chemistry to basalts from Apollo 12 and 15, but is enriched in light REE and has an unusually high Th/Sm ratio. Some Apollo 14 basalts yield a closer match to NWA 032 in REE patterns, but have higher concentrations of Al_2O_3. Ar-Ar step release results are complex, but yield a whole-rock age of ~2.8 Ga, suggesting that NWA 032 was extruded at 2.8 Ga or earlier. This rock may be the youngest sample of mare basalt collected to date. Noble gas concentrations combined with previously collected radionuclide data indicate that the meteorite exposure history is distinct from currently recognized lunar meteorites. In short, the geochemical and petrographic features of NWA 032 are not matched by Apollo or Luna samples, nor by previously identified lunar meteorites, indicating that it originates from a previously unsampled mare deposit.

Detailed assessment of petrographic features, olivine zoning, and thermodynamic modelling indicate a relatively simple cooling and crystallization history for NWA 032. Chromite-spinel, olivine, and pyroxene crystallized as phenocrysts while the magma cooled no faster than 2 °C/h based on the polyhedral morphology of olivine. Comparison of olivine size with crystal growth rates and preserved Fe-Mg diffusion profiles in olivine phenocrysts suggest that olivine was immersed in the melt for no more than 40 days. Plumose textures in groundmass pyroxene, feldspar, and ilmenite, and Fe-rich rims on the phenocrysts formed during rapid crystallization (cooling rates ~20 to 60 °C/h) after eruption.

Prelude preprint MS#4544

INTRODUCTION

Apollo and Luna missions have returned ~382 kg of rock and regolith from known locations on the Moon. Additional samples of the Moon are provided by lunar meteorites (*e.g.*, Marvin, 1983), but these are rare and were launched from unspecified locations on the Moon. In spite of these drawbacks, lunar meteorites comprise an important source of data to complement the returned Apollo and Luna samples and remote sensing observations in developing a more complete understanding of lunar processes and origin. The data on the Apollo and Luna samples represent a restricted equatorial region on the lunar nearside (Warren and Kallemeyn, 1991a), which, in light of remote sensing data, appears to be anomalously enriched in incompatible heat-producing elements (KREEP) compared to the average lunar surface (Jolliff *et al.*, 2000; Korotev, 2000; Lawrence *et al.*, 2000). Thus, these samples are biased to a restricted region and may be biased in composition as well. Lunar meteorites may originate from regions not sampled by the Apollo and Luna missions and, therefore, can be used to develop a more representative geochemical data set from which to evaluate lunar petrogenesis.

In this paper, we describe a newly found lunar meteorite, Northwest Africa (NWA) 032. It was found in the Sahara Desert in October 1999 as a fragment of ~300 g. It is the third unbrecciated meteorite from the lunar maria and is geochemically and petrographically distinct from the previously identified lunar mare meteorites, Yamato-793169 (Y-793169) and Asuka-881757 (A-881757, originally referred to as Asuka-31) (Yanai and Kojima, 1991). Nor do any of the Apollo or Luna samples match the geochemical and petrographic properties of NWA 032. Thus, NWA 032 is from a previously unsampled mare deposit.

The goals of this work are to document the Moon as the parent body of NWA 032, compare this meteorite with previously collected rocks from the lunar maria, and describe some constraints on its volcanic petrogenesis and shock history. We present data on the mineralogy, textures, mineral chemistry, major and minor element whole-rock chemistry, oxygen isotopic composition, cosmic-ray exposure ages, and $^{40}Ar/^{39}Ar$ isotopic results.

ANALYTICAL METHODS

Two polished thin sections of NWA 032 were examined using petrographic microscopes. Mineral modes were estimated from two point counts, one in reflected ($n = 2164$) and one in transmitted ($n = 2250$) light. A thin section scale, color x-ray map of Al, Fe, and Si Kα was used to help distinguish phases during point counting. The step size between points was ~20 μm.

Backscattered electron (BSE) images, elemental x-ray maps, and quantitative analyses of phases were collected using a Cameca SX-50 electron microprobe at the University of Hawai'i and a Cameca MBX electron microprobe at Northern Arizona University. Well-characterized oxide and silicate standards were used for quantitative wavelength dispersive analyses. Analyses were collected using a focused (~1 μm spot size), 15 keV, 10 or 20 nA beam, counting for 20 or 30 s on peak and background positions. The two microprobes yielded consistent results, but in order to avoid any complications resulting from instrument bias, only results from the UH microprobe are reported in this manuscript. We recognize that Ti^{3+} and Cr^{2+} may be present, particularly in lunar pyroxene, but we cannot detect directly the valence state of these elements from our microprobe data. It would be possible to estimate valence states by a difference calculation of the cation total after normalization to 6 oxygen, as is done for Fe-valence estimates in terrestrial pyroxenes. However, the abundances of Ti and Cr are so low (averaging under 2.5 wt% as TiO_2 and under 1.0 wt% as Cr_2O_3) that errors in this type of calculation could result in extremely misleading estimates of Ti and Cr valence state. Thus, we have normalized oxide and silicate mineral formula assuming that Ti and Cr are present as Ti^{4+} and Cr^{3+}. However, normalization of several pyroxene analyses under these assumed valences deviate from perfect stoichiometry in a trend suggestive of some Ti^{3+} and Cr^{2+} (see "Mineralogy and Textures").

The major element composition of NWA 032 was determined from aliquots of 0.55 g (major elements) and 52 mg (Na and K) using wet chemical methods outlined by Jarosewich (1990). Model crystallization of a liquid of NWA 032 major element composition was examined using MELTS (Ghiorso *et al.*, 1994; Asimow and Ghiorso, 1998) and experimentally determined partition coefficients (Roeder and Emslie, 1970). Minor and trace element concentrations were determined by instrumental neutron activation analysis (INAA) using procedures similar to those of Korotev (1991). Four fragments, with masses of 59, 41, 34, and 50 mg, were broken from separate portions of the meteorite and each fragment was subdivided further into two to four splits for analysis by INAA. In this work, mass-weighted mean concentrations representing the all splits (184 mg) are presented in the figures and tables; details of results for individual splits are available in Korotev *et al.* (2001).

A chip and a few fragments from a sawed slab with no visible fusion crust were prepared for oxygen isotopic and noble gas analyses. The oxygen isotopic composition of NWA 032 was determined using methods of Clayton and Mayeda (1963, 1983). Noble gas concentrations were determined from two samples of 22.31 and 22.80 mg. Noble gas extraction was conducted by radio frequency heating in a Mo crucible using the mass spectrometer system B at the University of Bern. All details concerning the instrument, analytical procedure, background, and blank corrections are described by Eugster *et al.* (1993).

Ar-Ar age determinations were made on samples G3 and G4 of NWA 032 (Table A1). The two samples were irradiated at the Sacavém reactor in Portugal with a fast neutron flux of

~2.4 × 10^{18} neutrons cm^{-2} (irradiation designated MN16). Samples were positioned between Hb3gr monitors in a silica vial. The difference in J value between the two monitors is 1% which is ~3× higher than the uncertainty in an individual J value. Therefore, a 1% uncertainty has been used in calculating individual step ages (Table A1) and 1.4% uncertainty in J, introduced from the error in the age determination of the monitor (1072 ± 11 Ma; Turner *et al.*, 1971), is included for calculation of the total ages given in Table A1. Experimental methods and data reduction procedures have been described previously (Burgess and Turner, 1998; Fernandes *et al.*, 2000). Argon blanks at low temperature (300–1000 °C) are 0.65 × 10^{-9} cm^3 STP ^{40}Ar and have an approximately atmospheric isotopic composition.

RESULTS

Mineralogy and Textures

Northwest Africa 032 is dominated by magmatic textures, with early-formed crystals of olivine, pyroxene, and chromite enclosed in a fine-grained crystalline groundmass of pyroxene, feldspar, ilmenite, troilite, and trace metal (Fig. 1; Table 1). In addition to these minerals, ulvöspinel occurs as rims around the chromite phenocrysts. Whole-rock shock-melt veins also occur.

Fractures due to terrestrial weathering occupy under 1% of the volume of NWA 032 (Fig. 1). In thin section, ~20% of the fractures occur as void space, and the remaining 80% have been filled with Ca-rich weathering precipitates. Detailed compositional and crystallographic data were not collected from the weathering products, but they appear to be dominated by Ca-carbonate with minor sulfate. Weathering products exhibit sharp textural boundaries with host rock phases, and no textural or compositional evidence of terrestrial oxidation or hydration in host rock phases, including metal and troilite, was detected. The weathering scale of Wlotzka (1993) was developed for ordinary chondrites, but is based on petrographic criteria that can be applied to NWA 032 and indicate a weathering grade of W0.

Chromite spinel formed early during the crystallization history of NWA 032; it may have been the first mineral to crystallize. It occurs as equant euhedral crystals up to ~80 μm across surrounded by groundmass minerals or included within olivine or pyroxene phenocrysts (Fig. 2). Chromite crystals are finer grained than the olivine and pyroxene phenocrysts, but are generally coarser than groundmass pyroxene, feldspar, and opaque minerals (Fig. 2). With this variation in grain size and in light of the early crystallization of chromite in NWA 032, we consider chromite part of the phenocryst assemblage (see Cox *et al.*, 1979, pp. 176–181 for discussion). Where chromite is surrounded by groundmass minerals, it is rimmed by ulvöspinel. Ulvöspinel rims have not been observed around chromite crystals fully included within olivine or pyroxene phenocrysts. Chromite interiors consistently yield analyses near the chromite endmember of the spinel solid solution, but with minor concentrations of TiO_2, MgO, and Al_2O_3 (Table 2; Fig. 3). Some of the coarser chromite crystals are zoned with Fe/(Fe + Mg) increasing from core (~0.75) to rim (~0.80), but most of the grains we analyzed exhibit minimal zoning. Much

TABLE 1. Modal abundances (vol%) in mare basalt meteorites and similar basalts from Apollo 12 and 15.

	Mare basalt meteorites				Apollo 12 and 15 basalts		
	NWA 032	Y-793169	A-881757	EET 87521* clast A	12016,25	12054	15556,136
Olivine phenocrysts	11.3	0	0	15	12.0	10.8	0.1
Chromite phenocrysts	0.3	0	<5	–	0.0	1.9	0.4
Pyroxene phenocrysts	4.8	–	–	–	–	–	–
Coarse pyroxene	4.8	–	–	–	–	–	–
Groundmass pyroxene	41.1	–	–	–	–	–	–
Undifferentiated pyroxene	50.7†	56	59	44	52.1	62.1	57
Feldspar	29.4	42	30	39	29.1	27.9	38
Silica	0.0	0	0	0	0.0	0.1	0.8
Volcanic glass/mesostasis	0.0	0	0	0	0.6	1.9	1.0
Ilmenite	4.4	1	6	2	4.8	5.2	2.1
Ulvöspinel	tr	1	<5	0	0.0	0.5	0.6
Troilite	0.7	0	<5	0	0.0	0.3	0.1
Metal	tr	0	<5	0	0.0	0.1	tr
Shock-melt glass	3.2	0	0	0	0.0	0.0	0.0

Data sources: NWA 032, this study; Y-793169, Takeda *et al.* (1993); A-881757, Yanai and Kojima (1991); Elephant Moraine (EET) 87251 clast A, Warren and Kallemeyn (1989); 12016 and 12054, Neal *et al.* (1994); 15556 from Rhodes and Hubbard (1973).
tr = present in trace abundance (identified in thin section, but not counted during point count).
*EET 87251 is a breccia with mafic lithic clasts.
†Undifferentiated pyroxene for NWA 032 = sum of phenocryst, coarse, and groundmass textural types.

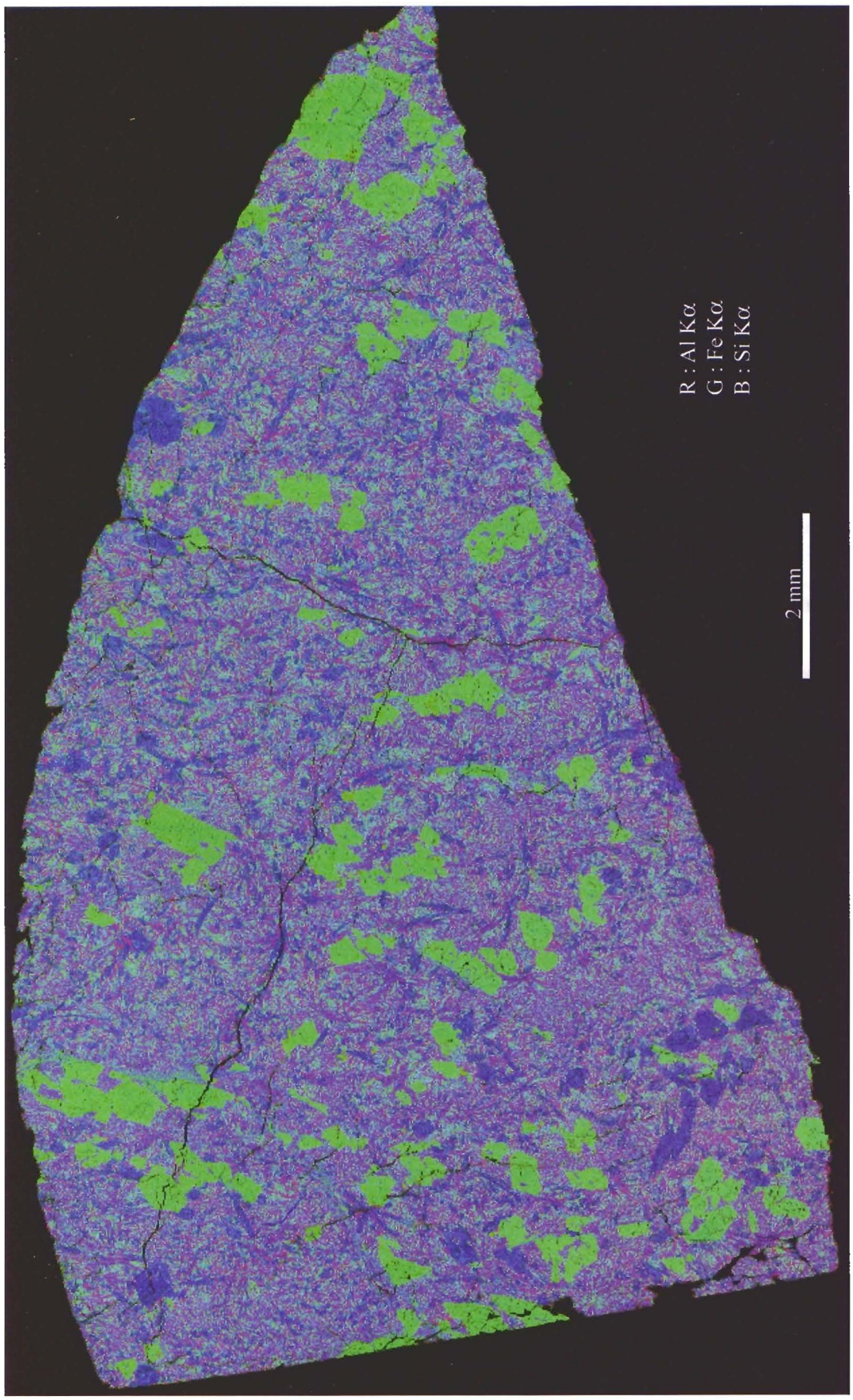

FIG. 1. X-ray map of a thin section of NWA 032: red = Al Kα; green = Fe Kα; blue = Si Kα. Pyroxene shows up both as relatively coarse-grained, dark blue (Mg-rich) and fine-grained light blue (Fe-rich) prisms. The green grains are olivine, and yellow-green grains are chromite. Red grains in groundmass are plagioclase. The cracks are weathering features partially filled with Ca-rich weathering minerals which appear dark on this image.

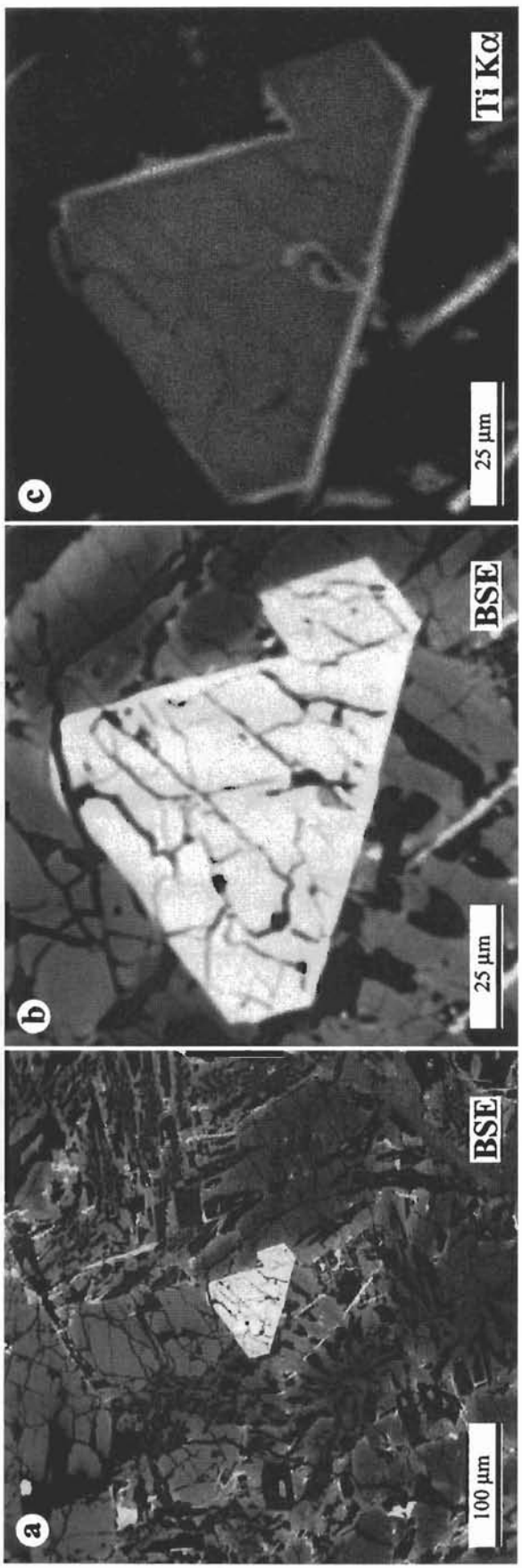

FIG. 2. Backscattered electron images (a and b) and Ti Kα x-ray map (c) of chromite with ulvöspinel rim. Note that the ulvöspinel rim is best developed at the interface between chromite and groundmass. Where the spinel margin is enclosed within a phenocryst (*e.g.*, lower right face of grain), the ulvöspinel rim is absent.

of the range in Fe/(Fe + Mg) observed in chromite in NWA 032 is from different compositions of different grains. The chromite interiors are euhedral, and exhibit sharp boundaries with ulvöspinel rims (Fig. 2). The rim compositions are nearly devoid of MgO, but have minor Al_2O_3 and Cr_2O_3, and are separated by a significant compositional gap from the cores (Fig. 3). The ulvöspinel rims exhibit a range in Cr/(Cr + Al) (Fig. 3), which may be due in part to overlap of the electron beam onto adjacent chromite. However, beam overlap alone, without a corresponding variation in Fe/(Fe + Mg), is not likely to cause the wide range in detected Cr/(Cr + Al), indicating that at least some of the range observed reflects a true variation in composition of the ulvöspinel.

Chromite and ulvöspinel compositions and textures in NWA 032 are relatively simple compared to complex textures and compositional trends observed in many mare basalts (*e.g.*, El Goresy *et al.*, 1976; Busche *et al.*, 1972). The chromites are euhedral, without corroded or resorbed margins, and the ulvöspinel rims are texturally and compositionally distinct. Similar textures in Apollo 12 and 15 pigeonite basalts have been interpreted as a result of chromite crystallizing in a melt followed by a cessation of crystallization followed in turn by late-stage precipitation of ulvöspinel (El Goresy *et al.*, 1976). The minor zoning observed in chromite in NWA 032 can be attributed to simple crystal growth in a melt becoming enriched in Fe/(Fe + Mg) during crystallization.

Olivine occurs as the most abundant and coarsest phenocryst, ranging up to 300 μm in apparent width in thin section, with equant to elongate crystal form (Figs. 1 and 4). Undulatory to mosaic extinction and microfaults offsetting phenocryst margins (Fig. 4) indicate that these crystals have been deformed. Spherical inclusions composed predominantly of very fine-grained pyroxene and feldspar were apparently trapped as melt inclusions (Fig. 5). Interiors of the olivine phenocrysts are broadly zoned from cores as Mg-rich as Fo_{66} to more Fe-rich compositions (~Fo_{50}) near crystal margins (Fig. 6). Phenocrysts with greater apparent width in thin section tend to have more forsteritic compositions in their interiors, indicating that the Fe-Mg zoning in olivine resulted from growth zoning, diffusive reequilibration after crystal growth, or some combination of primary growth and post-crystallization diffusion (Fig. 6). The continuously-zoned interiors are surrounded by thin (~1 to 3 μm) Fe-rich (~Fo_{15} to Fo_{30}) rims (Figs. 4 and 6). The compositional break between continuously zoned Mg-rich olivine interiors and Fe-rich rims is discontinuous within the spatial resolution of the electron microprobe. Ratios of Fe/Mn are similar to those identified in lunar olivine (Fig. 7).

Pyroxene is the most abundant phase in NWA 032 (Table 1) and exhibits a continuous variation in grain size from phenocrysts comparable in size to the coarse olivine phenocrysts down to finely tapered elongate crystals <1 μm in apparent width. For this study, we recognize three textural types of pyroxene and refer to them as follows: (1) crystals

TABLE 2. Representative electron microprobe analyses (wt%) of minerals and shock-melt glass in Northwest Africa 032.

Phase	Shock-melt glass	Chromite	Ulvö-spinel	Ilmenite	Olivine (interior)	Olivine (Fe-rim)	Ca-poor pyroxene (interior)	Ca-pyroxene (interior)	Pyroxene from (Fe-rim)	Ground-mass pyroxene	Ground-mass plagioclase
SiO_2	42.7	0.29	0.17	1.86	36.2	32.5	51.2	49.2	45.4	45.3	50.0
Al_2O_3	8.75	12.3	1.87	0.48	<0.02	0.20	1.43	2.87	2.21	2.44	30.4
TiO_2	2.76	5.80	32.4	49.9	0.04	0.19	0.62	1.2	1.83	2.63	0.16
Cr_2O_3	0.35	44.3	0.63	<0.04	0.28	<0.04	0.73	1.02	0.07	0.04	<0.04
FeO	24.5	31.3	63.4	46.4	33.8	52.9	19.2	16.2	34.5	33.7	1.76
MnO	0.29	0.20	0.33	0.35	0.29	0.48	0.36	0.27	0.49	0.44	<0.04
MgO	10.3	5.18	0.26	0.04	29.4	13.9	18.3	15.3	4.05	6.40	0.33
CaO	8.92	0.07	0.23	0.53	0.35	0.67	8.09	13.1	10.9	8.68	15.6
Na_2O	0.37	<0.02	<0.02	<0.02	<0.02	<0.02	<0.02	0.035	<0.02	<0.02	1.29
K_2O	0.09	<0.02	<0.02	0.054	<0.02	<0.02	<0.02	<0.02	<0.02	<0.02	0.08
Total	99.1	99.4	99.3	99.6	100.3	100.9	100.0	99.3	99.4	99.7	99.7
		Structural formala based on									
		4 O	4 O	3 O	4 O	4 O	6 O	6 O	6 O	6 O	8 O
Si^{4+}	–	0.010	0.006	0.047	0.994	0.987	1.93	1.88	1.89	1.86	2.30
Al^{3+}	–	0.491	0.082	0.014	b.d.	0.007	0.064	0.129	0.108	0.118	1.65
Ti^{4+}	–	0.148	0.911	0.943	0.001	0.004	0.018	0.035	0.057	0.081	0.006
Cr^{3+}	–	1.19	0.019	b.d.	0.006	b.d.	0.022	0.031	0.002	0.001	b.d.
Fe^{2+}	–	0.889	1.98	0.975	0.776	1.34	0.606	0.516	1.20	1.16	0.068
Mn^{2+}	–	0.006	0.010	0.007	0.007	0.012	0.011	0.009	0.017	0.015	b.d.
Mg^{2+}	–	0.262	0.015	0.002	1.21	0.629	1.03	0.872	0.251	0.391	0.022
Ca^{2+}	–	0.003	0.009	0.014	0.010	0.022	0.327	0.537	0.484	0.381	0.770
Na^+	–	b.d.	b.d.	b.d.	b.d.	b.d.	b.d.	0.003	b.d.	b.d.	0.115
K^+	–	b.d.	b.d.	0.002	b.d.	b.d.	b.d.	b.d.	b.d.	b.d.	0.005
Total	–	3.00	3.01	2.01	3.00	3.01	4.01	4.01	4.00	4.00	4.93
$Si+^{iv}Al$*	–	–	–	–	–	–	1.994	2.000	1.993	1.976	3.945
^{vi}Al*	–	–	–	–	–	–	0.000	0.007	0.000	0.000	0.000
fo/wo/an†	–	–	–	–	0.61	0.32	0.17	0.28	0.25	0.20	0.87
en/ab†	–	–	–	–	–	–	0.53	0.45	0.13	0.20	0.13

b.d. = below detection.

*Tetrahedral Si + Al, and octahedral Al shown for pyroxenes and feldspar only.

†Anorthite and albite contents are approximations, as the feldspar deviates from An-Ab-Or stoichiometry.

coarser than ~100 μm in width as phenocrysts; (2) finely tapered elongate crystals intercalated with feldspar as fine groundmass pyroxene; and (3) elongate grains of intervening size as intermediate. Admittedly, this classification is imperfect, but it calls attention to the true variation in grain size of pyroxene in NWA 032. Phenocryst, intermediate, and fine groundmass pyroxenes are distinct in composition as well as texture, and the phenocrysts and intermediate grains have multiple compositional domains, but most of the pyroxene analyzed can be classified as augite and the remainder as pigeonite.

Pyroxene phenocrysts are equant to slightly elongate, and are characterized by undulatory to mosaic extinction. Three compositional domains can be discerned from BSE images: (1) dark (in BSE) phenocryst cores; (2) mantles which are slightly lighter in BSE grayscale than the cores; and (3) BSE-bright Fe-rich rims similar to the thin rims that surround olivine phenocrysts (Fig. 5). Multiple analyses of the phenocrysts shown in Fig. 5 indicate that the subtle BSE contrast between cores and mantles results from minor differences in Mg/(Mg + Fe) (molar) of 61 to 66 in the cores to Mg/(Mg + Fe) of 55 to 60 in the mantles (Fig. 8a). Core compositions vary considerably in Ca (Wo_{10} to Wo_{40}), but Mg/(Mg + Fe) is relatively constant. No gap in Ca content between augite ($Wo_{>20}$) and pigeonite ($Wo_{<20}$) is apparent. Pyroxene compositions from phenocryst mantles vary in Mg/(Mg + Fe) as well as Ca content (Fig. 8a) and generally exhibit continuous zoning toward more Fe-rich compositions closer to crystal margins. The rims are significantly more Fe-rich than the phenocryst interiors and tend to have relatively low Ca contents (Fig. 8a). The rims have higher Mg/(Mg + Fe) and Ca content than pure pyroxferroite (Fig. 8a), a late-stage, Ca,Fe-pyroxenoid observed in several Apollo mare basalts (Chao *et al.*, 1970; Papike *et al.*, 1976). Both pyroxene and olivine have Fe-rich rims where phenocrysts are in contact with groundmass minerals (in some

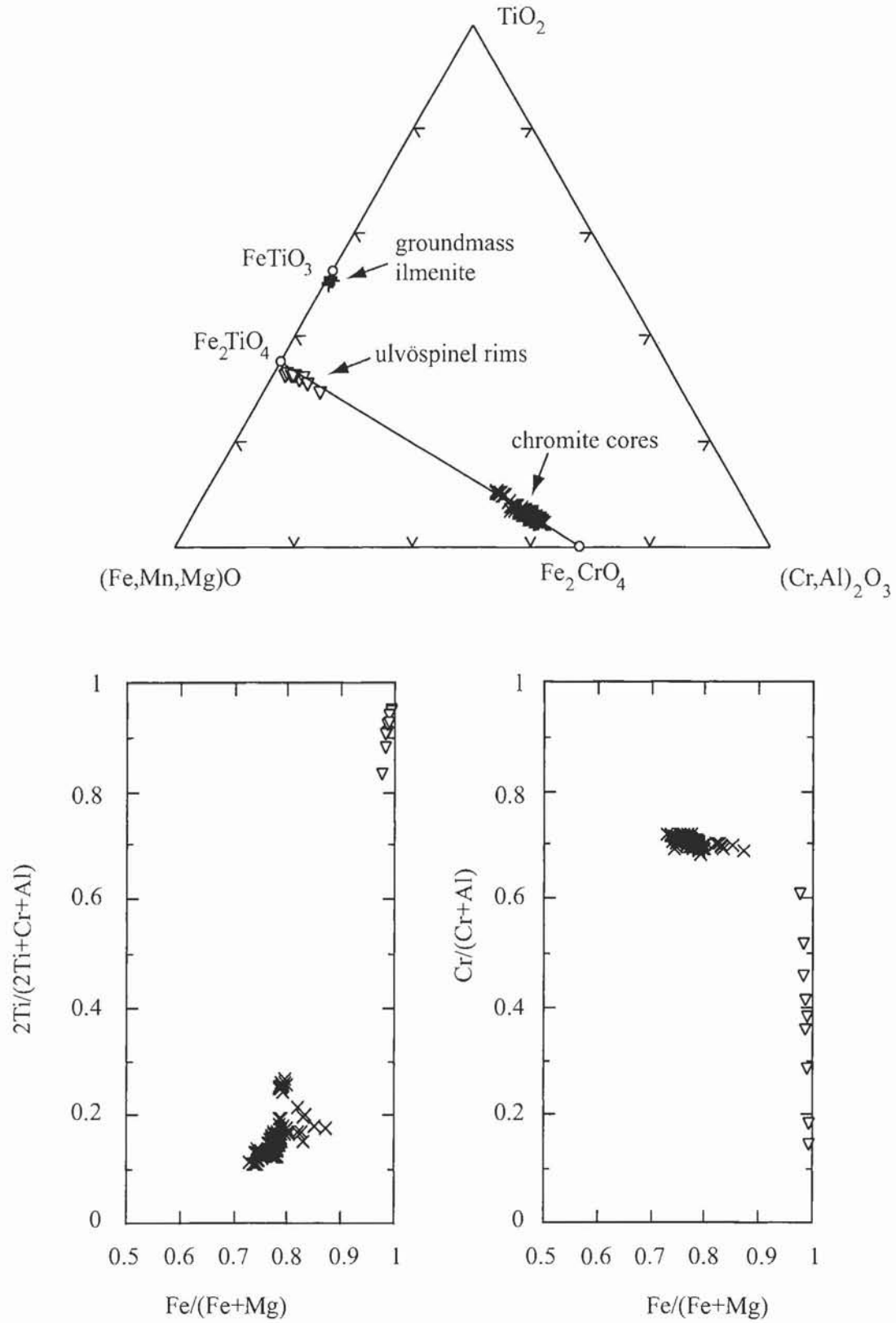

FIG. 3. Compositions of chromite phenocrysts with ulvöspinel rims (a, b, c) and ilmenite (a only) from NWA 032: (a) weight percent ternary plot of El Goresy *et al.* (1971); (b) and (c) molar ratio plots of Busche *et al.* (1972). Plots are based on electron microprobe analyses of ilmenite ($n = 9$) from the groundmass, and rims ($n = 9$) and cores ($n = 166$) of spinel solid solution phenocrysts. Phenocryst core and rim compositions fall near chromite and ulvöspinel endmembers and are resolved from each other by a large compositional gap (see Fig. 2). Analytical errors (1σ) due to counting statistics are smaller than symbols.

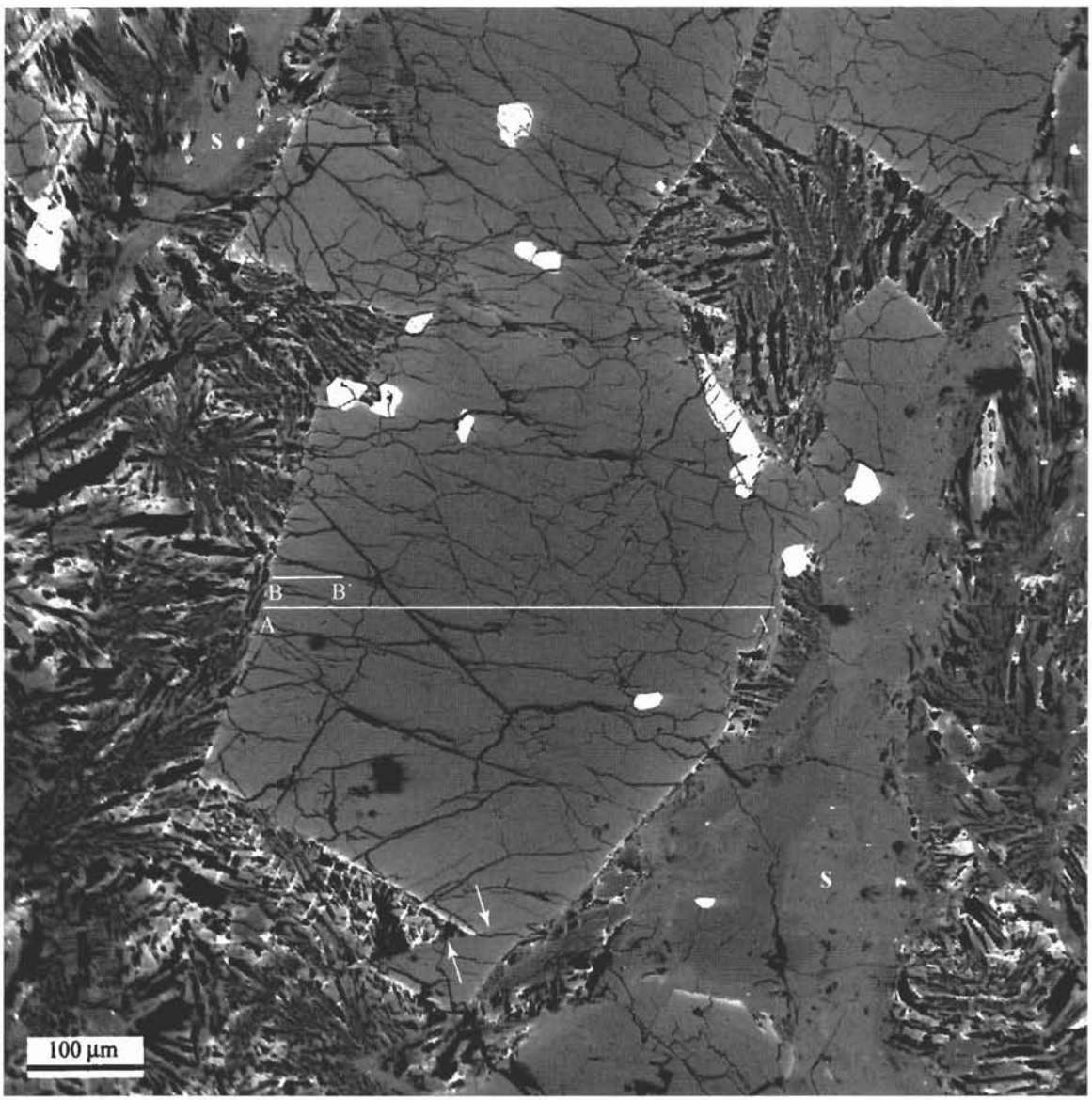

FIG. 4. Backscattered electron image of zoned olivine phenocryst and adjacent materials. Subtle dark to light gray variation from core to rim of phenocryst at center reflects continuous zoning from magnesian core (~Fo_{66}) to less magnesian rim (~Fo_{60}). Lines A–A' and B–B' denote positions of compositional profiles shown in Fig. 6. Thin bright seam around olivine consists of very Fe-rich (~Fo_{22}) rim. Bright equant crystals, mostly included in olivine, are chromite. Arrows highlight microfault in olivine. Shock veins (s) are present along the right margin and upper left corner of image. Fine-grained groundmass minerals consist mostly of pyroxene (medium gray) and feldspar (black), which occur in radial splays and elongate dendritic patterns. Fine elongate prisms of ilmenite (white) are prominent in the groundmass below the central olivine phenocryst.

cases, the distinction between groundmass pyroxene and rim pyroxene cannot be made), but Fe-rich rims are absent where olivine and pyroxene phenocrysts have been sutured together (Fig. 5).

Core, mantle, and rim domains are distinct in Al, Ti, and Cr as well as the quadrilateral components. Mantles are enriched in high field-strength elements, with $\Sigma(Al,Ti,Cr) \approx 0.3$ atoms per 6-oxygen formula unit (apfu) in contrast to $\Sigma(Al,Ti,Cr) \approx 0.17$ in the cores and ~0.14 in the rims. Aluminum in the cores appears to have been introduced into the pyroxene structure by both Tschermak ($AlAlMg_{-1}Si_{-1}$) and coupled titanian ($TiAl_2Mg_{-1}Si_{-2}$) exchange reactions (Thompson, 1982), resulting in Ti/Al of 1/4 (Fig. 9a). Ratios of Ti/Al in the mantles form a trend toward higher concentrations of Ti and Al, with Ti/Al increasing, suggesting a gradual increase in ratio of coupled titanian to Tschermak exchange reactions. In contrast, rim domains are separated by a compositional gap, with lower concentrations of Ti and Al, and Ti/Al near 1/2, suggesting no Tschermak exchange in the rims. The values of Ti/Al greater than 1/2 cannot be attained under the normalization assumptions used in this study, but are possible if some Ti^{3+} is present (Bence and Papike, 1972).

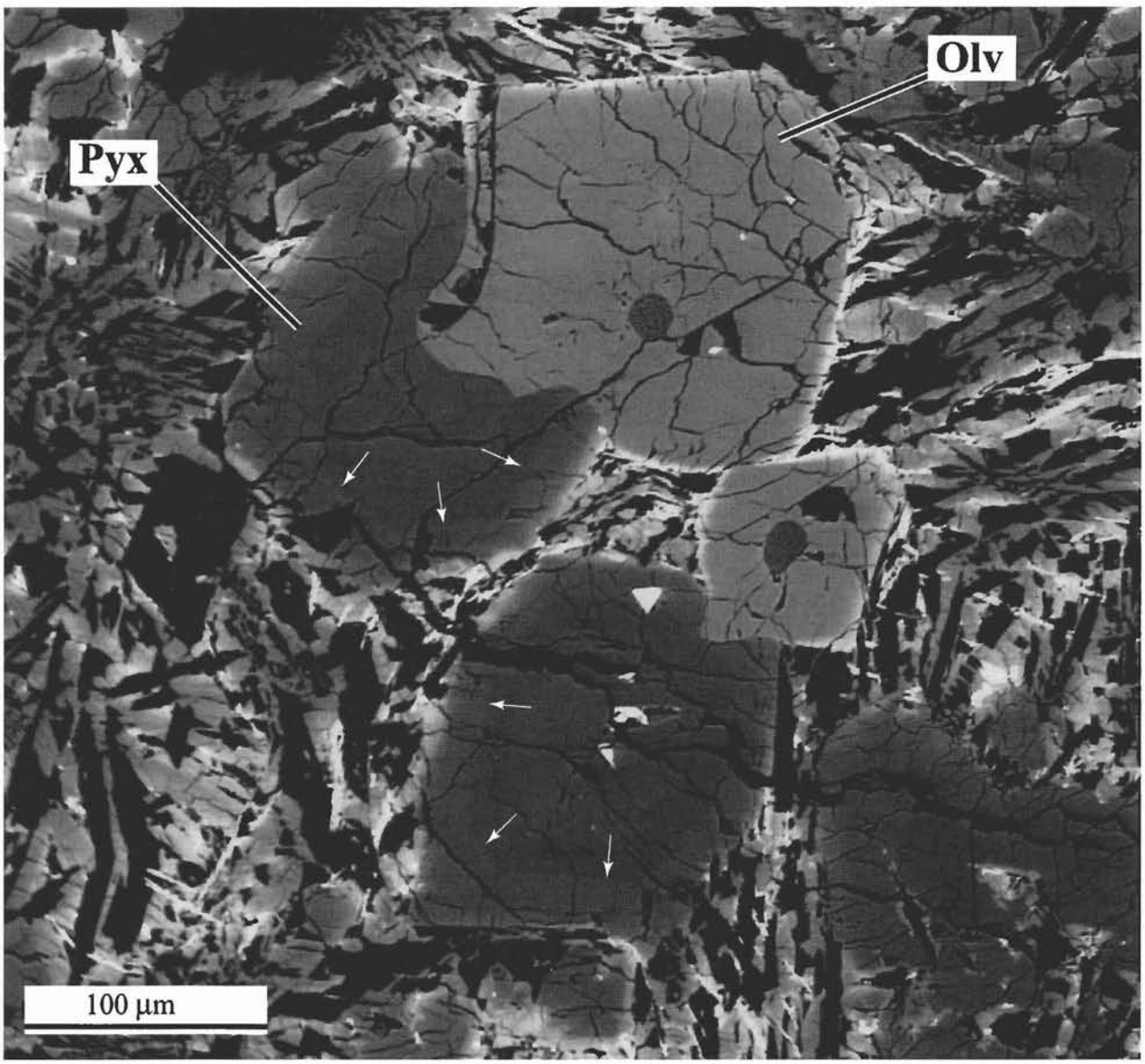

FIG. 5. Backscattered electron image of joined pyroxene (Pyx) and olivine (Olv) phenocrysts. A thin, Fe-rich (bright gray to white) quenched rim is present along phenocryst faces in contact with groundmass minerals. No such rim is present along the interface between the phenocrysts. A subtle but discontinuous break in grayscale in the pyroxene phenocrysts (see arrows) reflects a compositional break from more Mg-rich compositions interior to the break to more Fe-rich compositions closer to phenocryst margins. Bright triangle-shaped inclusion in lower pyroxene phenocryst is chromite. Spherical to subspherical inclusions in olivine are melt inclusions that consist now of very fine-grained pyroxene and feldspar similar to the groundmass. Groundmass minerals consist of feldspar (black), continuously zoned pyroxene (shades of medium gray), and ilmenite and troilite (both white in this image).

Similar compositional jumps in pyroxene Ti/Al values from 1/4 to 1/2 have been linked to the onset of feldspar crystallization in other mare basalts (Bence and Papike, 1972).

Pyroxenes classified as intermediate are <50 μm in width, exhibit more elongate crystal form in thin section than the phenocrysts, and are coarser than adjacent feldspar crystals. Many, but not all, intermediate-sized pyroxene grains have distinct Fe-rich rims. Some analyses of the interior portions of intermediate pyroxene yield Mg-rich, Ca-poor compositions similar to the phenocryst cores, but most of the intermediate pyroxene is similar in composition to the phenocryst mantles in both Wo-En-Fs components (Fig. 8b) and high field-strength elements (Fig. 9b). The thin Fe-rich rims on intermediate-sized pyroxene grains are compositionally similar to the Fe-rich phenocryst rims and much of the fine groundmass pyroxene (Figs. 8 and 9).

Fine groundmass pyroxene occurs as elongate crystals interstitial with plagioclase feldspar. In some cases, pyroxene and feldspar occur as radial splays emanating from common nucleation sites ("plumose texture", Fig. 10a). Fine pyroxene crystals lack quenched rims but are zoned continuously over large ranges in Mg, Fe, Ca and high field-strength elements

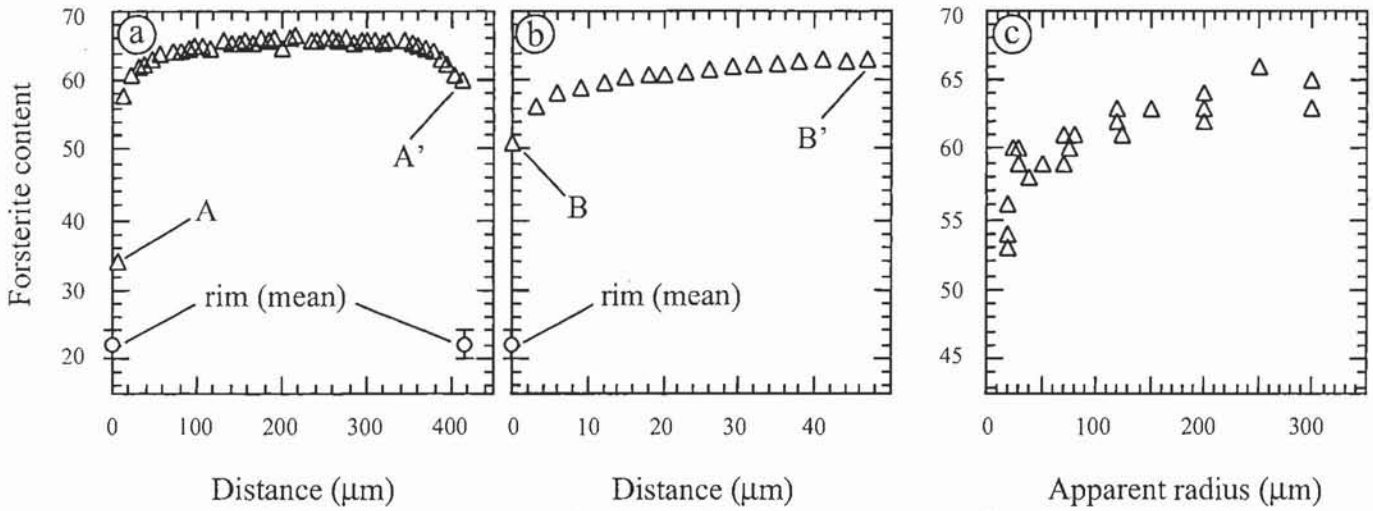

FIG. 6. Fe-Mg zoning profiles in olivine phenocryst (a) and (b), and relationship between apparent radius and maximum Fo-content in olivine (c). Profiles (a) and (b) are from olivine phenocryst shown in Fig. 4. Mean composition of rim is based on five analyses of the thin Fe-rich rim surrounding the continuously zoned interior. Profile (c) is based on maximum Fo content determined from multiple analyses in cores of 27 olivine phenocrysts, and the apparent radius (or, for elongate crystals, width) in thin section. Analytical uncertainties (1σ) due to counting statistics are smaller than the symbols.

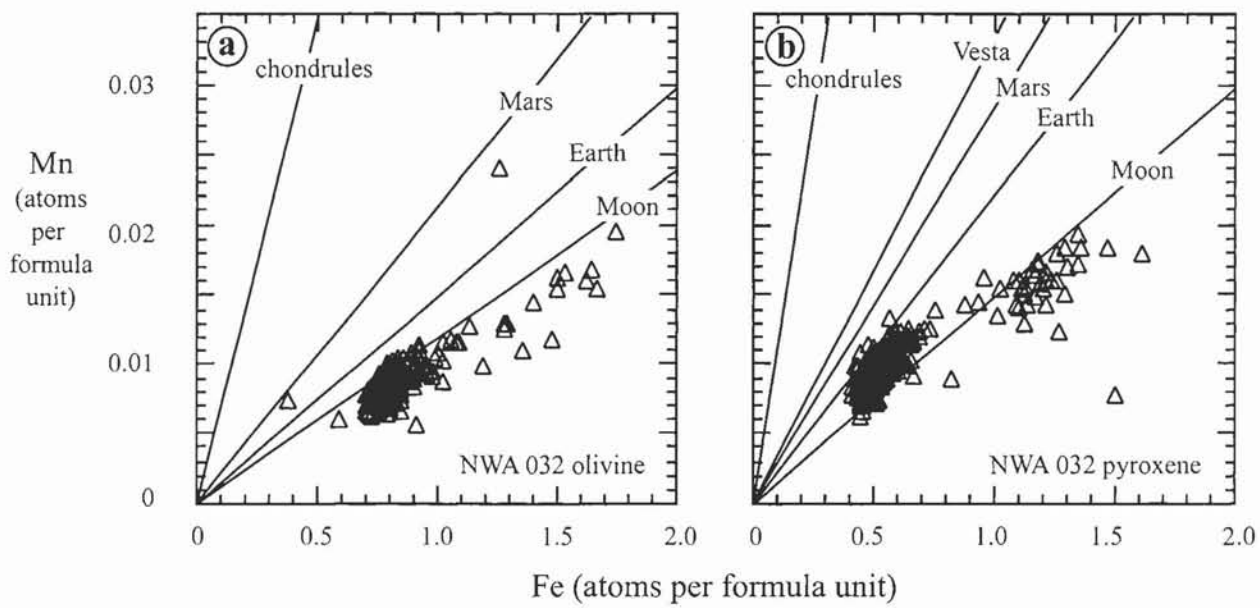

FIG. 7. Concentrations of Fe and Mn in olivine (a) and pyroxene (b) from NWA 032. Atoms per formula unit are based on 4 oxygen for olivine and 6 oxygen for pyroxene. Ratios of Fe/Mn associated with specific parent bodies are from Papike (1998). Analytical uncertainties (1σ) due to counting statistics are smaller than the symbols.

(Figs. 8c and 9c). Some groundmass pyroxene is extremely Fe-rich, with Mg/(Mg + Fe) near 0 (Fig. 8c).

Electron microprobe analyses of fine, intermediate, and phenocryst pyroxene yield nearly stoichiometric mineral formulae when normalized with all Fe assumed to be ferrous. As discussed above, better stoichiometry can be attained in several cases if some cations, perhaps Cr or Ti, have lower valences than we have assumed for normalization. Although these results do not constitute a direct observation of the Fe oxidation state, it is strong evidence, particularly in light of the low oxygen fugacities implied by the presence of Fe-metal in the groundmass, that all Fe in NWA 032 pyroxene is ferrous. Ratios of Fe/Mn are similar to those identified in lunar pyroxenes (Fig. 7).

Plagioclase feldspar is abundant in the groundmass of NWA 032 (Table 1), where it forms fine elongate tapered crystals between pyroxene crystals of similar size and form (Figs. 4 and 10). Because of the fine grain size, feldspar crystallinity is difficult to assess; however, at least some of the feldspar appears to be maskelynite. Feldspar compositions typically range between An_{80} and An_{90}, but have excess Ca and Si relative to Na, K, and Al for ideal An-Ab-Or feldspar stoichiometry (Table 2). It is unlikely that the deviations from stoichiometry are due to loss of alkalies during microprobe

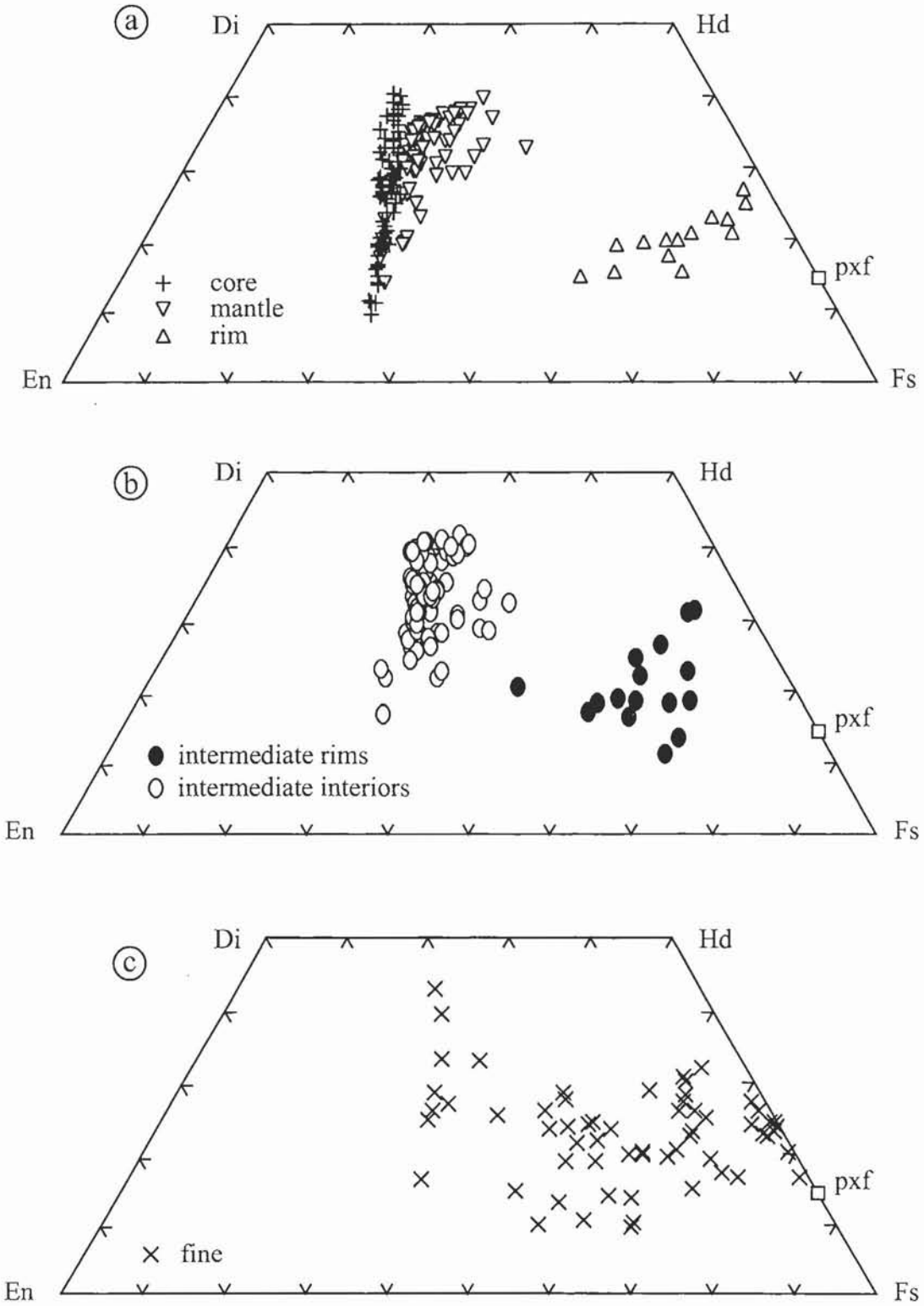

FIG. 8. Pyroxene quadrilateral compositions of phenocryst (a), intermediate-sized (b), and fine groundmass (c) pyroxene from NWA 032. Some analyses of groundmass pyroxene approach the idealized composition of pyroxferroite (pxf), but in general, analyses are distributed over a wide compositional range. Core (n = 75), mantle (n = 79), and rim (n = 14) compositions plotted in (a) are from the pyroxene phenocrysts shown in Fig. 5. Analyses of interior portions (n = 89) and Fe-rich rims (n = 16) of intermediate-sized grains and fine (n = 61) pyroxenes are from several areas in the thin section examined in detail (Fig. 1). Analytical uncertainties (1σ) due to counting statistics are smaller than the symbols.

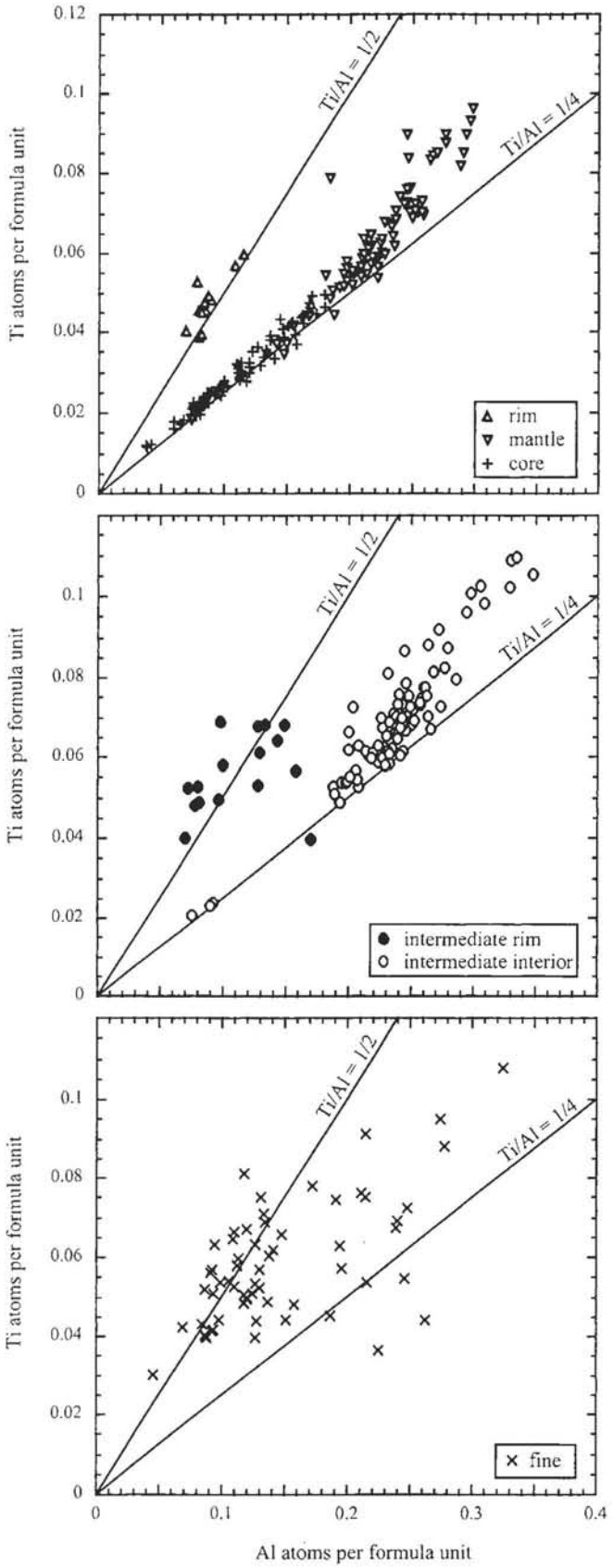

FIG. 9. *(right)* Atoms per formula unit (6 oxygen normalization) Ti *vs.* Al in pyroxene for phenocrysts (a) shown in Fig. 5, intermediate-sized grains (b), and fine pyroxene interstitial with plagioclase feldspar in the groundmass (c). Wo-En-Fs components of these analyses are plotted in Fig. 8. A Ti/Al ratio of 1/2 can be accounted for by substitution of $TiAl_2Mg_{-1}Si_{-2}$ exchange component into an endmember composition (or "additive component" of Thompson, 1991) of $CaMgSi_2O_6$. A Ti/Al ratio of 1/4 requires another exchange component, and can be accounted for by substitution of one $^{vi}Al^{iv}AlMg_{-1}Si_{-1}$ ("Tschermak exchange", see for example Thompson, 1982) for every $TiAl_2Mg_{-1}Si_{-2}$. Values of Ti/Al greater than 1/2 are not possible by these exchange components and suggest that some Ti^{3+} may be present (Bence and Papike, 1972). Shifts from Ti/Al $\approx$ 1/4 to Ti/Al > 1/4 may denote the onset of feldspar crystallization (Bence and Papike, 1972). Analytical uncertainties (1σ) due to counting statistics are smaller than the symbols.

analyses, because a relatively low current (10 nA) was used, and alkali-loss during analysis results in excess Al relative to alkalies (*e.g.*, Morgan and London, 1976), in contrast to our results. The relatively high concentrations of Mg and Fe in addition to Ca and Si are similar to several previously analyzed mare feldspars (Crawford, 1973), and suggest that charge balance is maintained by substitution of Ca, Mg, Fe, and Si into the alkali-deficient feldspar (Wenk and Wilde, 1973; Longhi *et al.*, 1976).

Opaque phases occur in the groundmass and include ilmenite, troilite, and rare metal (Table 2). Both ilmenite and troilite are widely dispersed and characteristic of the groundmass, whereas only six tiny (radii ≤ 1 μm) metal grains were identified in the thin section shown in Fig. 1. Ilmenite is the most abundant opaque phase and forms elongate branching crystals typically no more than 3 μm in width (Fig. 10b). Textures indicative of subsolidus reduction (see El Goresy and Ramdohr, 1975) were not observed in ilmenite in NWA 032; however, subsolidus textures may be difficult to recognize in this case because of the fine, elongate, branching texture of the ilmenite. Troilite is commonly found adjacent to ilmenite and forms equant grains no more than 3 or 4 μm across.

Shock veins are widely dispersed in the meteorite. They consist of whole-rock shock-melted glass with basaltic composition (Table 2) and fragmented mineral inclusions (Fig. 4). Micro-faults are common in the rock and have caused offsets of phenocrysts and groundmass minerals (Figs. 4 and 10b). We attribute the micro-faults, maskelynitization of feldspar, and undulatory extinction in olivine and pyroxene to shock deformation.

Whole-Rock Composition: Major and Minor Elements and Oxygen Isotopes

Northwest Africa 032 is a basalt with whole-rock Fe/Mn ratio in the range of lunar meteorites and returned lunar samples (Table 3). Multiple analyses by INAA yield a mean FeO concentration of 22.1 $\pm$ 0.2 (1σ) wt%, which is slightly lower than the value of 23.0 wt% determined by wet chemical methods (analyst, E. Jarosewich) (Table 3). The discrepancy

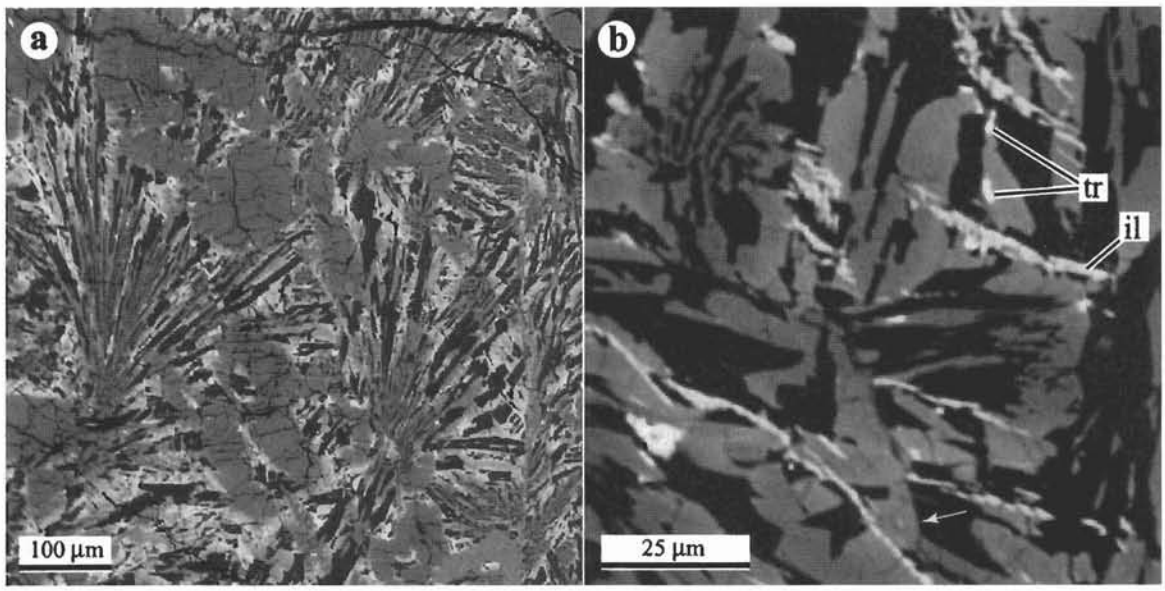

FIG. 10. Backscattered electron images of groundmass textures in NWA 032. (a) Plumose texture of elongate pyroxene (medium gray) and feldspar (dark gray) radiating away from common nucleation sites. (b) Elongate dentritic morphology of ilmenite (il) in contrast to equant form of troilite (tr). From darkest to lightest in grayscale, minerals in this image consist of feldspar, pyroxene, ilmenite, and troilite. Variable grayscale of pyroxene reflects continuous zoning in Fe, Mg, and Ca.

between results may have resulted from analytical errors, or from heterogeneities in primary composition, or weathering effects of the different specimens analyzed. In either case, the FeO concentration of NWA 032 is among the highest of lunar mare samples (Table 3).

Based on its low TiO_2, Al_2O_3, and K_2O concentrations (Table 3), NWA 032 is classified as a low-Ti basalt, similar to basalts from Apollo 12 and 15 (Neal and Taylor, 1992). The concentration of Al_2O_3 *vs.* MgO in NWA 032 falls along major element trends consistent with olivine fractionation in olivine basalts from both Apollo 12 and 15 (Fig. 11). The concentration of TiO_2 also is consistent with the Apollo 12 trend, but falls above the values observed in Apollo 15 samples. However, the major elemental composition of NWA 032 does not appear to fit in any of the Apollo 12 suites: it is TiO_2-poor compared to the ilmenite basalts; FeO-rich and SiO_2-poor compared to the pigeonite basalts; and has higher FeO/MgO at similar SiO_2 concentration in comparison to the olivine basalts.

Thermodynamic modeling of a cooling liquid of NWA 032 whole-rock composition produces minerals and mineral compositions similar to those observed in the meteorite. Partition coefficients determined by Roeder and Emslie (1970) indicate that olivine precipitating from a liquid of NWA 032 composition has an equilibrium composition of Fo_{65}, matching the composition of the interiors of the coarsest (earliest formed) olivines (Fig. 6). A low-pressure (1 bar) model crystallization sequence based on MELTS (Ghiorso *et al.*, 1994; Asimow and Ghiorso, 1998) predicts that spinel should crystallize first from a cooling liquid of NWA 032 composition at 1223 °C, followed by olivine at 1184 °C and pyroxene at 1180 °C, consistent with the crystallization sequence inferred from textures. In the MELTS model, the initial pyroxene has a composition of $Wo_{08}En_{63}$, similar to the composition of the most Ca-poor pyroxene detected in phenocryst cores in NWA 032 (Fig. 8). With continuing crystallization, model pyroxene becomes more Ca- and Fe-rich, consistent with trends of pyroxene composition in the meteorite.

Analyses of multiple fragments broken from different portions of the meteorite indicate that it is compositionally homogeneous with respect to minor elements (Korotev *et al.*, 2001). Rare earth element (REE) concentrations yield a well-defined Eu anomaly typical of lunar mare basalts (Table 3; Fig. 12). Higher bulk concentrations of REE, a light rare earth element (LREE)-enriched pattern, and a deeper Eu anomaly distinguish NWA 032 from the Apollo 12 and 15 basalts and A-881757. The LREE-enriched pattern of NWA 032 is similar to patterns observed in high-Al basalts from Apollo 14.

The Th/Sm ratio of NWA 032 is unusually high in comparison to previously sampled mare basalts (Fig. 13). We believe that the high Th/Sm ratio is not the result of terrestrial alteration for two reasons. First, although there is evidence for chemical alteration in Dar al Gani 262 (Bischoff *et al.*, 1998) and Dhofar 025 (Taylor *et al.*, 2001; Warren *et al.*, 2001), Th/Sm ratios in these meteorites (0.37 and 0.36) are not significantly different from those in feldspathic lunar meteorites from Antarctica (0.33 in Allan Hills (ALH) A81005, Kallemeyn and Warren, 1983; 0.34 in MacAlpine Hills 88015, Warren and Kallemeyn, 1991b; 0.35 in Y-86032, Warren and Kallemeyn, 1991a) or feldspathic Apollo soils (mean 0.36 in soils from North Ray Crater at Apollo 16, Korotev, 1996). Second, the relative standard deviation of Th/Sm ratios in 12 subsamples of NWA 032 analyzed by INAA is 2.8%, virtually

TABLE 3. Elemental composition of mare-rich meteorites and similar basalts from Apollo 12 and 15.

	Lunar mare meteorites					Apollo 12 and 15 basalts			
	NWA 032 NMNH	NWA 032 WUSL*	Y-793169 (1)	A-881757 (1)	EET 87521 (2)	12016,9 (3)	12054,62 (3)	15119,19 (4)	15556, 177 (4)
wt%									
SiO_2	44.7	–	46.0	47.1	48.4	42.8	45.9	44.9	45.7
TiO_2	3.08	–	2.19	2.45	1.13	4.02	4.63	2.57	2.62
Al_2O_3	8.74	–	11.1	10.0	12.5	7.23	10.5	8.96	9.48
Cr_2O_3	–	0.401	0.24	0.29	0.21	0.57	0.33	0.587	0.838
FeO	23.0	22.1	21.2	22.5	19.2	22.6	19.5	22.2	21.7
MnO	0.33	–	0.32	0.34	0.24	0.3	0.29	0.28	0.28
MgO	8.45	–	5.75	6.30	6.30	12.7	6.76	9.38	8.15
CaO	10.9	–	12.0	11.8	11.7	8.42	11.9	10.0	10.6
Na_2O	0.37	0.347	0.27	0.25	0.41	0.22	0.31	0.26	0.257
K_2O	0.11	–	0.06	0.04	0.07	0.06	0.07	0.048	0.047
Total	99.7	–	99.2	101.0	100.0	98.89	100.16	99.23	99.60
Mg/(Mg + Fe)†	39.6	–	32.6	33.3	37.3	49.9	38.2	43.0	40.1
Fe/Mn†	69.8	–	66.0	66.0	78.5	75.5	67.3	79.3	77.4
μg/g									
Sc	–	56	93.7	99.4	44	–	–	44	46
Co	–	42	29.8	27.9	46	54	31	50	50
Ni	–	50	53	52	29	25	–	59	63
Sr	–	142	78	115	104	126	162	112	101
Zr	–	175	59	45	140	117	128	95	94
Ba	–	242	34	27	88	59	64	44	44
La	–	11.2	4.72	3.69	8.3	–	–	5.36	5.2
Ce	–	29.7	14.8	10.9	20.9	16.2	18.8	15.9	15.8
Nd	–	21	11.9	8.31	13	–	–	15	13
Sm	–	6.61	4.30	2.88	3.86	5.5	6	3.82	3.65
Eu	–	1.10	1.31	1.10	0.98	1.06	1.27	0.94	0.96
Tb	–	1.56	1.02	0.76	0.8	1.42	1.85	0.83	0.87
Yb	–	5.79	4.59	3.26	3.19	5	5.8	2.36	2.27
Lu	–	0.802	0.66	0.52	0.48	0.67	0.78	0.32	0.31
Hf	–	5.00	3.01	2.20	2.88	6.3	4.8	2.89	2.89
Ta	–	0.62	0.31	0.22	0.37	–	–	0.41	0.39
Au (ng/g)	–	4	1.1	0.2	<1.2	–	–	–	–
Th	–	1.90	0.68	0.42	0.95	–	–	0.49	0.46
U	–	0.45	0.09	0.16	0.23	–	–	–	–

Analyses of NWA 032 conducted by wet chemical methods at the U. S. National Museum of Natural History (NMNH) and by INAA at Washington University, St. Louis (WUSL). Other analyses: (1) major elements from Warren and Kallemeyn (1993), and minor elements from Koeberl *et al.* (1993); (2) Warren and Kallemeyn (1989); (3) Rhodes *et al.* (1977); (4) Ryder and Schuraytz (2001).
*WUSL results are mass-weighted means of 12 analyses from 4 subsamples of NWA 032 (Korotev *et al.*, 2001).
†By convention, Fe/Mn is calculated from concentrations by weight, whereas Mg/(Mg + Fe) is molar.

identical to the mean estimated 1σ analytical uncertainty, 3.1% (Korotev *et al.*, 2001). If terrestrial alteration affected the Th/Sm ratio, we would not expect it to have done so uniformly. The high concentration of Au (4 ng/g), in contrast, is almost certainly the result of terrestrial contamination.

The whole-rock oxygen isotopic composition of $\delta^{18}O = +5.63‰$ and $\delta^{17}O = +2.92‰$ is consistent with a lunar origin. This composition falls along the terrestrial fractionation line in the field of lunar (and terrestrial and enstatite meteorite) rocks. However, the oxygen isotopic composition does not provide a constraint on the lunar region or geologic setting from which NWA 032 originates.

Argon-Argon Ages

Results of the stepped heating Ar isotopic analysis of fragments G3 and G4 are given in Table A1. Age spectra, Ca/K and cosmic-ray exposure ages of the individual steps are shown

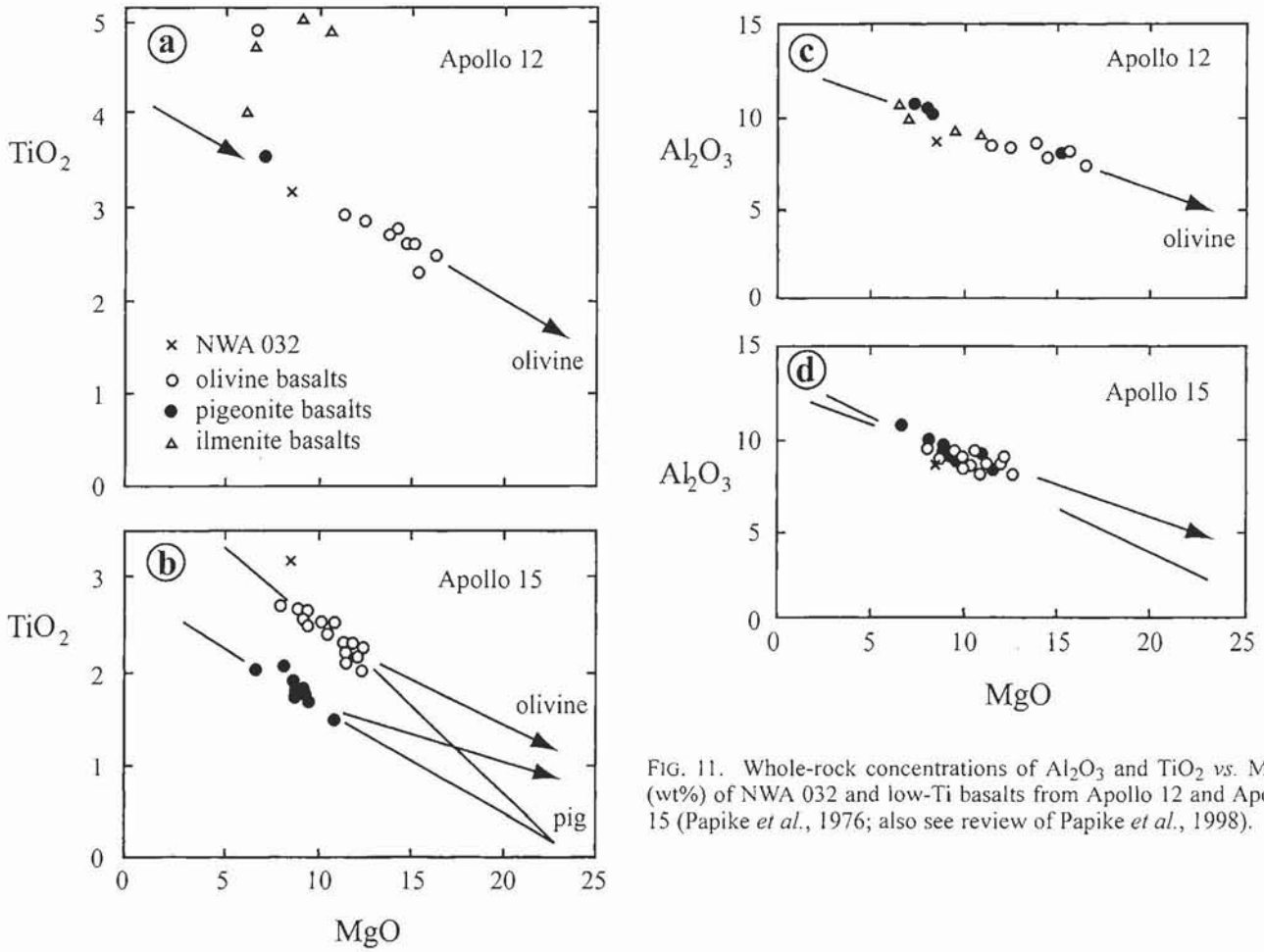

FIG. 11. Whole-rock concentrations of Al_2O_3 and TiO_2 *vs.* MgO (wt%) of NWA 032 and low-Ti basalts from Apollo 12 and Apollo 15 (Papike *et al.*, 1976; also see review of Papike *et al.*, 1998).

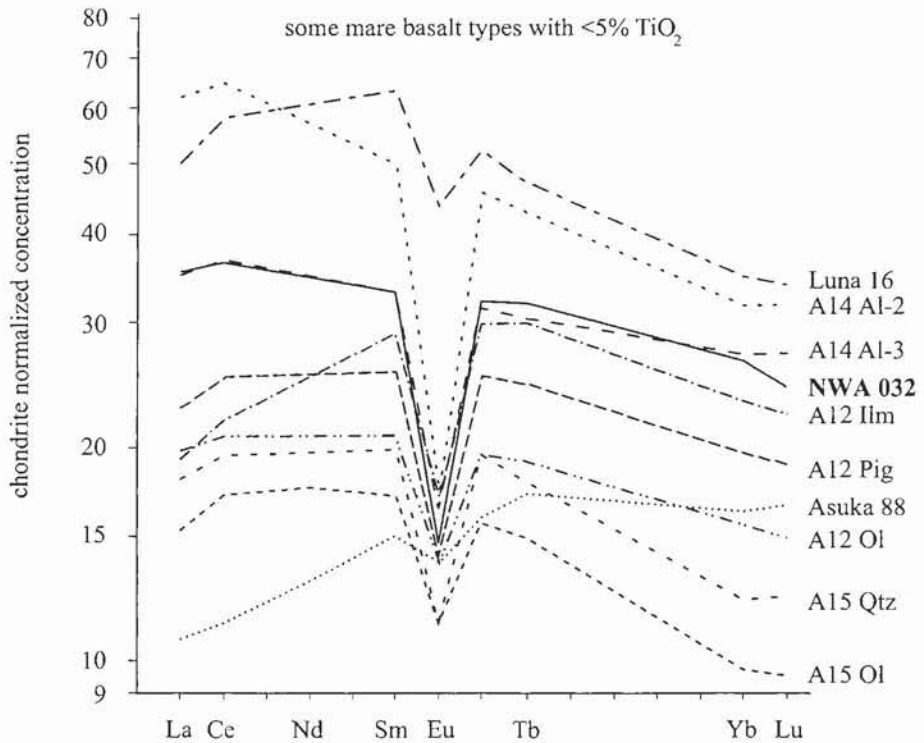

FIG. 12. Rare earth element concentrations of NWA 032 (normalized to volatile-free CI chondrites) compared with other low-Ti mare basalts.

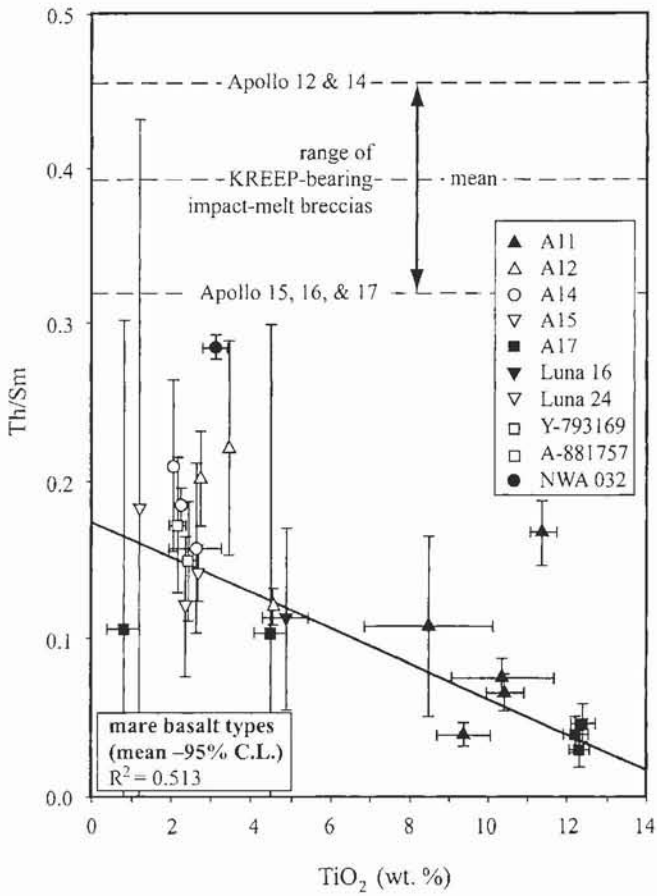

FIG. 13. Variation of Th/Sm with TiO_2 in mare basalts. The error bars represent 95% confidence limits and the diagonal line is a least-squares fit weighted by the confidence limits. There is a weak tendency for Th/Sm to decrease with increasing TiO_2. NWA 032 has an unusually high Th/Sm ratio.

in Fig. 14. The $^{38}Ar/^{36}Ar$ ratios in all but the lowest and highest temperature steps are very close to that expected for cosmogenic argon (1.54) and both samples contain negligible amounts of solar Ar. This is the same as found previously for two other lunar mare basalt meteorites, A-881757 and Y-793169 (Thalmann *et al.*, 1996), and is consistent with the fact that NWA 032 is an unbrecciated mare basalt which does not contain regolith components exposed to the solar wind.

The age spectra show a complex pattern; there is evidence for a small amount of ^{40}Ar loss at low temperatures, thereafter the apparent ages rise to a maximum of 3.3–3.5 Ga at 400–500 °C accounting for 10–14% of the ^{39}Ar release (Fig. 14). Apparent ages decline steadily to 2.4–2.8 Ga at intermediate release (30–60% of the ^{39}Ar release) before finally falling again at high temperature. The Ar-Ar release patterns are similar to those obtained from some fine-grained Apollo 14 rocks (Turner *et al.*, 1971) where the high-temperature apparent ages do not seem to date any geologic event, but the total Ar-Ar ages agree with the Rb-Sr ages and appear to be meaningful (whether the Rb-Sr ages represent igneous crystallization or impact melting has been questioned recently; see Snyder and Taylor, 2001). The total Ar release ages obtained for G3 and G4 are indistinguishable at 2.775 ± 0.092 and 2.800 ± 0.020 Ga, respectively. Subsequent analyses of multiple fragments by infrared-laser single-shot gas extraction yield similar ages, and a third step-heating profile is similar to the profiles from G3 and G4 (Fernandes *et al.*, 2001); these new data will be described in detail in a forthcoming manuscript and are consistent with results presented here. Two possible interpretations of the causes and chronological implications of the complex age spectra are discussed below.

(1) During the irradiation, recoil of ^{39}Ar from fine-grained K-rich plagioclase to K-poor pyroxene may lead to artificially high ages at low temperatures and low ages from high-temperature release from pyroxene (Turner and Cadogan, 1974). The increase in Ca/K (Fig. 14b) from ~4 to ≥300 with increasing release temperature suggests that the low-temperature releases were dominated by Ar from plagioclase and whole-rock shock-melted glass veins, whereas the high-temperature releases were dominated by Ar from pyroxene. The extremely fine-grained texture of the K-bearing phases indicates that ^{39}Ar recoil is a plausible mechanism influencing the Ar release. If this is the case, then the total Ar age of 2.80 Ga can be interpreted as having geological significance, possibly indicating the time of the original crystallization. The age might alternatively represent the timing of a major impact responsible for the formation of the melt veins. However, it seems more likely that the melt veins are a recent feature associated with the ejection of NWA 032 from the lunar surface and that this event did not affect the K-Ar systematics significantly.

(2) Ar-Ar laser probe measurements of melt glass in the Peace River meteorite (McConville *et al.*, 1988) indicated that radiogenic argon can be retained preferentially in shock-produced melt glass that is rapidly quenched. If this occurred during formation of the shock-melt veins in NWA 032, then it is possible that the highest step ages represent partial retention of radiogenic argon by the melt glass and the intermediate release ages of 2.4–2.8 Ga record the time of thermal annealing following the impact. As with (1) above, this interpretation, that the ages date a post-impact annealing episode, can be discounted if the veins are related to ejection of the meteorite from the Moon.

The $^{38}Ar/Ca$ ratios are high in the low-temperature steps (Fig. 14c), possibly due to the presence of Cl-derived ^{38}Ar from terrestrial contaminants. The $^{38}Ar_c/Ca$ from step releases above 800 °C, corresponding to ~90% of the ^{37}Ar release and inferred to be dominantly from pyroxene, shows little variation with weighted mean values for G3 = (2.042 ± 0.108) × 10^{-6} cm^3/g Ca and G4 = (2.056 ± 0.194) × 10^{-6} cm^3/g Ca. Using the method of Eugster and Michel (1995) adjusted for 2π geometry, we calculate a production rate of ^{38}Ar from calcium of 0.905 × 10^{-8} cm^3 STP/g/Ma, corresponding to exposure ages of 226 ± 12 Ma and 227 ± 13 Ma for G3 and G4, respectively, where errors are analytical precision and do not account for uncertainties in production rate. These values are within error

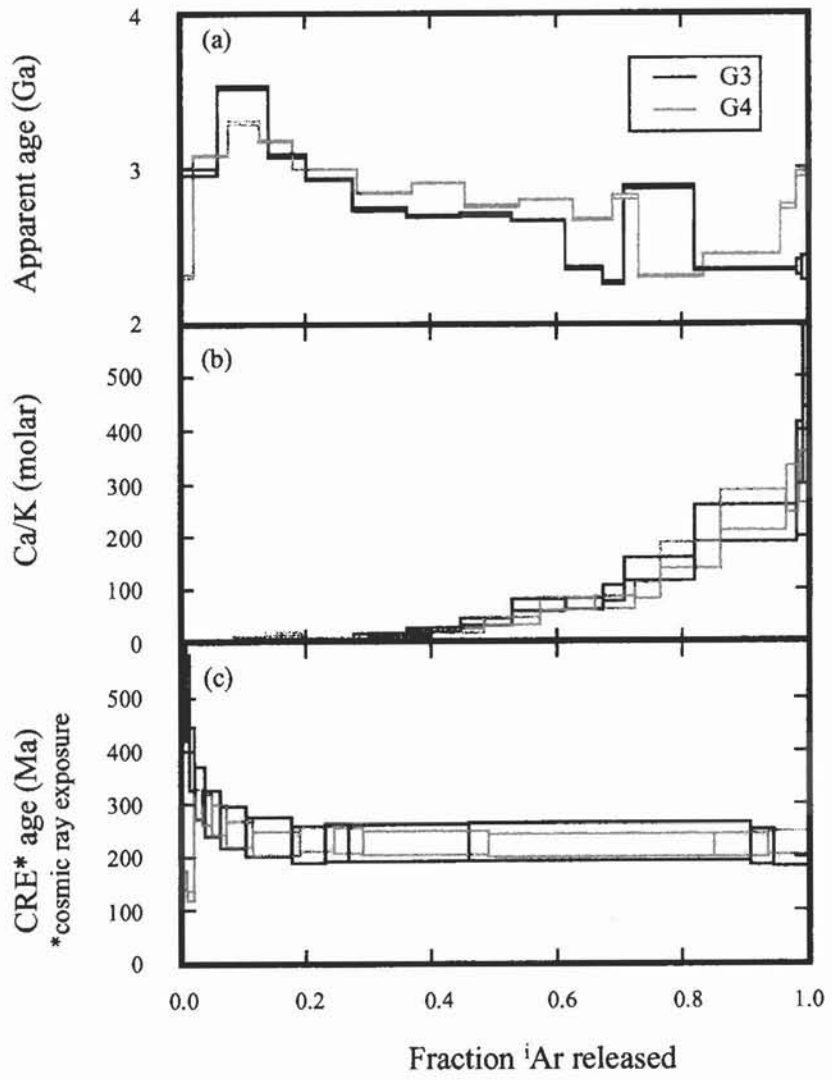

FIG. 14. ^{40}Ar-^{39}Ar step-heating results for samples G3 and G4 of NWA 032 fragments G3 and G4. (a) Apparent age *vs.* ^{39}Ar released. (b) Ca/K ratio (molar) *vs.* ^{39}Ar released. (c) Cosmic-ray exposure age *vs.* ^{37}Ar released.

of cosmic-ray exposure ages determined from gases extracted by radio frequency heating (see below).

Cosmic-Ray Exposure Ages

Noble gas concentrations used for deriving the cosmic-ray exposure history of NWA 032 are presented in Table 4. In order to determine cosmic-ray exposure ages, production rates for cosmogenic ^{21}Ne and ^{38}Ar must be derived. These production rates depend on the chemical composition of the investigated material (Table 3) and on shielding depth during exposure to cosmic rays. The cosmogenic ratio $^{22}Ne/^{21}Ne = 1.144$ indicates that the NWA 032 material was irradiated at a shielding depth of a few tens of centimeters. Using the method for calculating production rates proposed by Eugster and Michel (1995) we obtain cosmic-ray exposure ages from ^{21}Ne and ^{38}Ar of ≥110 Ma. Nishiizumi and Caffee (2001) measured the radionuclides ^{41}Ca, ^{10}Be, ^{26}Al, and ^{36}Cl, and calculated a Moon–Earth transfer time of ~0.05 Ma. Therefore, we conclude that the cosmic-ray irradiation occurred when the NWA 032 material resided in the lunar regolith. In that case, the production rates have to be adjusted to a 2π exposure geometry, and we obtain an average lunar regolith residence time of 220 ± 30 Ma (Table 5). The relatively low concentrations of trapped solar wind ^{20}Ne are consistent with the low solar Ar (see "Argon-Argon Ages") and indicate that the NWA 032 is an interior sample of a rock never exposed directly at the very top of the lunar surface. Using the concentration of 2370×10^{-8} cm^3 STP/g for radiogenic ^{40}Ar (Table 5) and a K concentration of 913 ppm (Table 3), we calculate an Ar retention age of 2775 ± 160 Ma, the error limits taking into account a 10% uncertainty for K. This K-Ar age is in excellent agreement with the total Ar-Ar ages of G3 and G4 given above.

TABLE 4. Results of He, Ne, and Ar measurements at University of Bern for NWA 032.

Sample	^{4}He	^{20}Ne	^{40}Ar	^{4}He	^{20}Ne	^{22}Ne	^{36}Ar	^{40}Ar
	(10^{-8} cm^3 STP/g)			^{3}He	^{22}Ne	^{21}Ne	^{38}Ar	^{36}Ar
22.31 mg	3675	17.61	2344	176.7	0.832	1.138	0.681	175.6
	±150	±0.70	±100	±2.0	±0.009	±0.012	±0.008	±3.0
22.80 mg	5168	19.00	2398	225.8	0.806	1.154	0.667	179.8
	±200	±0.80	±100	±2.0	±0.008	±0.012	±0.008	±3.0
Average	4420	18.30	2371	201.2	0.819	1.146	0.674	177.7
	±180	±0.70	±100	±2.0	±0.008	±0.012	±0.008	±3.0

Errors are 2σ.

TABLE 5. Cosmogenic, radiogenic, and trapped noble gases calculated from data in Table 4, cosmic-ray exposure (CRE) and K-^{40}Ar ages, and lunar regolith residence time of NWA 032.

Cosmogenic ^{21}Ne	$(19.5 \pm 1.0) \times 10^{-8}$ cm^3 STP/g
Cosmogenic ^{38}Ar	$(19.7 \pm 1.0) \times 10^{-8}$ cm^3 STP/g
Cosmogenic ^{22}Ne/^{21}Ne	1.144 ± 0.010
Radiogenic ^{4}He	$(4300 \pm 200) \times 10^{-8}$ cm^3 STP/g
Radiogenic ^{40}Ar	$(2370 \pm 100) \times 10^{-8}$ cm^3 STP/g
Solar wind ^{20}Ne	$<0.7 \times 10^{-8}$ cm^3 STP/g
CRE age from ^{21}Ne	208 ± 30 Ma
CRE age from ^{38}Ar*	232 ± 30 Ma
Lunar regolith residence time	220 ± 30 Ma
K-^{40}Ar age	2775 ± 160 Ma

*This value, based on gas extractions by radio frequency heating, is within error of CRE ages of 226 ± 12 Ma and 227 ± 13 Ma, determined from step-heating Ar isotopic analyses.

DISCUSSION

Lunar Origin and Age

Multiple lines of evidence indicate a lunar origin of NWA 032. The oxygen isotopic composition falls in the field of terrestrial and lunar rocks, and enstatite chondrites and achondrites. An enstatite meteorite parent body can be ruled out because all mafic silicates in NWA 032 have considerable Fe in solid solution with Mg. The presence of Fe,Ni metal, troilite and ilmenite, and the absence of ferric iron indicate petrogenesis under oxygen fugacities lower than terrestrial basalts, ruling out a terrestrial origin. Ratios of Mn/Fe in the whole rock, pyroxenes, and olivines all are consistent with lunar origin (Table 3; Fig. 7), as is the low-alkali content of plagioclase. Pyroxene in the groundmass and along Fe-rich quenched rims of phenocrysts may be extremely Fe-rich; these Fe-rich compositions are typical of lunar pyroxenes, but are not characteristic of pyroxenes from terrestrial basalts. The deep Eu anomaly of NWA 032 is typical of other lunar mare samples.

The Ar-Ar data, though difficult to interpret, are dominated by step releases with apparent ^{40}Ar/^{39}Ar ages ranging from 2.5 to 3.5 Ga (Fig. 14) and total ages ~2.8 Ga, somewhat young in comparison to returned mare samples, but reasonably associated with the timing of the later stages of mare volcanism (Schmitt, 1991; Hiesinger *et al.*, 2000). If NWA 032 lost radiogenic Ar during shock metamorphism, then the true volcanic age is older than 2.8 Ga (see "Argon-Argon Ages") and may be closer in age to returned mare samples. Alternatively, as discussed above, the whole-rock Ar-Ar age may represent the volcanic age of NWA 032; if so, this rock is one of the youngest currently available samples of mare basalt.

Further evidence for a lunar origin comes from the cosmic-ray exposure history determined from cosmogenic nuclides (Nishiizumi and Caffee, 2001) and noble gases (this study). Exposure to cosmic rays in the lunar regolith for 220–230 Ma and a Moon–Earth transfer time of 0.05 Ma, as determined for NWA 032, are typical of lunar meteorites.

Comparison with Other Mare Basalts

General geochemical similarities of NWA 032 to other mare rocks indicate a lunar origin, but in detail, the geochemistry and mineralogy of NWA 032 are sufficiently distinct to indicate that this meteorite originates from a previously unsampled mare basalt. With the exception of its low Al_2O_3 content, NWA 032 is similar in major element composition to the other unbrecciated mare meteorites, Y-793169 and A-881757 (Table 2); however, neither Y-793169 nor A-881757 has olivine phenocrysts (Table 1), and both of these meteorites are much coarser grained than NWA 032 (Yanai and Kojima, 1991). Furthermore, cosmic-ray exposure ages derived from noble gases (this study) and cosmogenic nuclides (Nishiizumi and Caffee, 2001) indicate that NWA 032 is distinct from these meteorites in ejection date from the Moon as well as exposure to cosmic rays on the lunar surface (Thalmann *et al.*, 1996).

The basaltic breccia Elephant Moraine (EET) 87521 was ejected from the Moon at a similar time as NWA 032, but has a different cosmic-ray exposure history (Vogt *et al.*, 1993). The brecciated texture and relatively low TiO_2 content of EET 87521 further distinguish this meteorite from NWA 032. One lithic clast in EET 87521 does have modal olivine (Table 1); however, this clast is coarser grained than NWA 032 (Warren and Kallemeyn, 1989).

NWA 032 shares similarities in major element composition with basalts from Apollo 12 and olivine-normative basalts from Apollo 15 (Table 3). In the scheme of Neal and Taylor (1992), the Apollo 12 (Rhodes *et al.*, 1977; Neal *et al.*, 1994a), Apollo 15 (Rhodes and Hubbard, 1973; Ryder and Schuraytz, 2001), and NWA 032 basalts all are classified as "low-Ti" basalts, with low concentrations of TiO_2, Al_2O_3 and K_2O (Table 3). In detail, however, geochemical and petrographic observations indicate that NWA 032 does not originate from the flows sampled during Apollo 12 and 15. Higher concentrations of REE and a deeper Eu anomaly distinguish NWA 032 from Apollo 15 basalts (Fig. 12). Furthermore, the modal abundance of olivine in NWA 032 is much higher than Apollo 15 samples of comparable major element composition (Table 1). We argue that NWA 032 originates from a lava that erupted with olivine phenocrysts (see "Crystallization Sequence and Volcanic Petrogenesis"), in contrast to the Apollo 15 olivine-normative basalts; thus, we infer that the differences in mode reflect distinct petrogenetic histories, not simple within-flow modal variations. The Apollo 12 ilmenite basalts produce a closer match to NWA 032 in modal mineralogy and trace element concentrations, but are relatively enriched in TiO_2 and depleted in REE (Tables 1 and 3; Fig. 12). Apollo 14 group 3 aluminous basalts are similar to NWA 032 in REE concentrations (Fig. 12), but have Al_2O_3 contents of 12.0 to 13.5 wt% (Dickinson *et al.*, 1985), in contrast to the low-Al composition of NWA 032 (Table 3).

NWA 032 has the highest Th/Sm ratio of known mare basalts (Fig. 13), further indicating that it represents a previously unsampled unit, and suggesting that some petrogenetic mechanism may fractionate Th from REE. Without a suite of samples it is difficult to assess the origin of the high Th/Sm, but it may involve the greater incompatability of Th in major basaltic minerals or a distinct source of melt. The high bulk concentrations of REE and LREE-enrichment observed in NWA 032 also are consistent with a distinct, possibly KREEP-like, source for the melt from which NWA 032 crystallized.

Using compositionally constrained, global remote sensing data—FeO = 18–22 wt% and Th = 1–3 ppm, Lunar Prospector gamma-ray spectrometer (Lawrence *et al.*, 2000); TiO_2 = 1.5–5 wt%, Clementine spectral reflectance (Lucey *et al.*, 2000)—the most likely source areas for NWA 032 are, in order of probability (on the basis of compositional match and areal extent): Mare Humorum, M. Fecunditatis, western M. Serenitatis, M. Crisium, and far western Oceanus Procellarum. However, if the whole-rock Ar-Ar age is the volcanic age of NWA 032 and if volcanism in M. Humorum ceased by 2.93 Ga (Hiesenger *et al.*, 2000), then Humorum cannot be the source of NWA 032.

Crystallization Sequence and Volcanic Petrogenesis

Chromite, olivine, and pyroxene phenocrysts in NWA 032 crystallized prior to the intermediate pyroxene and groundmass minerals. Forsterite contents of the coarsest (earliest-formed) olivine phenocrysts match the compositions of olivines predicted to crystallize from a melt of NWA 032 composition (Roeder and Emslie, 1970). This observation is evidence that the olivine phenocrysts crystallized *in situ* without significant accumulation, and implies that NWA 032 is similar in whole-rock major element composition to the liquid from which it formed. This interpretation is supported by MELTS (Ghiorso *et al.*, 1994; Asimow and Ghiorso, 1998) modeling, which predicts a crystallization sequence and pyroxene compositional trends consistent with observations from the meteorite.

The olivine phenocrysts are particularly informative about crystallization history. The zoning preserved in olivine phenocrysts (Fig. 6) provides a lower limit on the cooling rate during growth, as infinitely slow growth or extended immersion of crystals in hot liquid would result in homogeneous compositions in olivine regardless of crystal size. Quantitative estimates of cooling rate from olivine zoning are based on assumed initial growth profiles and require iterative calculations (Onorato *et al.*, 1978) which were not conducted as a part of this study. However, a limit on the length of time olivine coexisted with liquid can be provided from average diffusion distances; calculations based on the constants of Chakraborty (1997) indicate that the coarsest olivine crystals should have been homogenized if the system remained near liquidus temperatures (~1220 °C at 1 atm) for more than ~40 days. The olivine phenocrysts have polyhedral form with rare "hopper" embayments, suggesting crystal growth at cooling rates slower than 2 °C/h (Donaldson, 1976). Sizes of the crystals combined with growth rates can be used to place limits on the time the magma spent in cooling reservoirs (magma chamber or dike) before eruption. Growth rates of silicate minerals have been determined for a variety of geologic materials, and vary generally from 10^{-8} to 10^{-10} cm/s, with no significant difference among plagioclase, pyroxene, and olivine (*e.g.*, Kirkpatrick, 1977; Cashman and Marsh, 1988; Cashman, 1993; Crisp *et al.*, 1994; Armienti *et al.*, 1994). Most results fall in the range from 10^{-8} to 10^{-9} cm/s, consistent with unpublished experimental data from G. Lofgren and G. J. Taylor. Growth rates vary inversely with cooling rate (Cashman, 1993), probably a reflection of differing extents of undercooling, and inversely with melt viscosity (Kirkpatrick, 1975). Assuming cooling rates somewhat less than 2 °C/h (based on the crystal shapes) and a viscosity for the NWA 032 magma of 3 Pa s (calculated at the liquidus temperature of 1220 °C), we assume growth rates between

10^{-7} and 10^{-8} cm/s. If correct, these rates indicate that the largest olivine crystals took 3.5 to 35 days to grow.

The sutured contacts between olivine and pyroxene phenocrysts (Fig. 5) indicate that these crystals grew simultaneously over at least part of their crystallization history. The similarities in composition between the phenocryst mantles and intermediate-sized pyroxene crystals in the groundmass suggest that these pyroxene domains crystallized simultaneously as well. The sharp boundaries between phenocryst cores and mantles (Fig. 5) suggest an abrupt change in physical conditions, such as eruption, followed by relatively rapid crystal growth to produce the normally zoned mantles. Phenocryst cores and mantles, and the interiors of intermediate-sized grains have low Ti/Al (Fig. 9), consistent with growth of these pyroxene domains in the absence of feldspar (Bence *et al.*, 1970). Higher Ti/Al in the Fe-rich rims and many groundmass pyroxenes and intergrowth textures indicate that these domains co-crystallized with feldspar.

The well-defined, compositionally distinct Fe-rich rims on chromite, olivine, and pyroxene phenocrysts, and the fine texture of groundmass minerals are evidence of rapid crystal growth during late-stage crystallization. However, the absence of volcanic glass indicates that cooling was not instantaneous. Care must be taken in inferring cooling rates from textures, because variations in undercooling, saturation levels, and abundance of nuclei in the parent liquid all may affect nucleation and crystal growth rates (Lofgren *et al.*, 1974; Lofgren, 1983). With this caveat, however, some constraints on cooling rates are plausible. The plumose texture of pyroxene and feldspar in the groundmass was reproduced experimentally in an analog of lunar basalts at cooling rates of ~20 to 60 °C/h (Lofgren *et al.*, 1974). These rates are an order of magnitude faster than the cooling rate estimated from olivine morphology over the early part of the crystallization history. Thus, an early slow cooling episode was followed by a stage of rapid cooling during the volcanic history of NWA 032.

The above discussion leads to the following petrogenetic history for lunar basalt NWA 032. Its parent magma formed by partial melting of a mantle with major mineralogy not much different from that inferred for the low-Ti olivine basalts from Apollo 12 and 15: olivine, orthopyroxene, and augite (Neal and Taylor, 1992; Neal *et al.*, 1994b). However, the relatively high REE contents of NWA 032 are distinct from the other low-Ti basalts, and may have resulted from dynamic mixing of late-stage magma ocean products (ur-KREEP) into the source. It is possible that fractionation during the formation of ur-KREEP or during its mixing with olivine- and pyroxene-rich mantle rocks caused the fractionation of Th from Sm (Fig. 13).

Once the magma left its source in the mantle, it ascended toward the surface in a dike. The moving magma in a confined dike would prevent early-crystallizing olivine and pyroxene from fractionating. During the dike transport phase the magma cooled at <2 °C/h, producing the observed olivine morphology. The magma experienced more rapid cooling upon eruption, producing the intermediate-sized pyroxene crystals and zoned mantles in the pyroxene phenocrysts. Rapid crystallization of the Fe-rich rims and fine-grained minerals of the groundmass followed nucleation of feldspar during late-stage volcanic cooling at the lunar surface. Rapid crystal growth compared to diffusion at this stage resulted in the compositional heterogeneities observed in ulvöspinel and groundmass pyroxenes.

Shock History

Shock-melt veins, maskelynitization of feldspar, undulatory to mosaic extinction in olivine and pyroxene phenocrysts, and microfaults offsetting phenocrysts and groundmass crystals all are attributed to shock. The paucity of shock effects in returned lunar mare samples suggests that shock effects in NWA 032 may have been caused by the impact event that ejected it from the Moon; if so, then the Ar-Ar ages were not reset by the impact. Impact experiments on a lunar basalt indicate that total maskelynitization of feldspar requires shock pressures near 40 GPa (Schaal and Hörz, 1977). Vesiculated feldspathic glass, which is not observed in NWA 032, occurs in basalts shocked experimentally as impact pressures approach 50 to 60 GPa (Schaal and Hörz, 1977; Stöffler *et al.*, 1988). Therefore, the impact that ejected NWA 032 from the Moon probably induced pressures in the range from 40 to 60 GPa. Of course, this pressure estimate must be considered with caution because a variety of initial conditions affect shock petrogenesis and excursions from equilibrium may occur during shock events (Stöffler *et al.*, 1988; Chen *et al.*, 1996).

CONCLUSIONS

Mineralogy, textures, and mineral and whole-rock compositional data indicate a lunar origin of NWA 032 and are consistent with a fairly simple crystallization history during dike transport and volcanic eruption. The petrologic and geochemical observations combined with Ar-Ar isotopic data and cosmic-ray exposure ages indicate that NWA 032 is from a previously unsampled mare deposit and, thus provides a new source of data for understanding mare volcanism and lunar processes in general. Future work may address some of the questions raised during this general study: (1) Is NWA 032 younger than previously collected mare basalts? (2) Are trace element compositions of NWA 032 phenocrysts consistent with our interpretation of crystallization during ascent and volcanic eruption? (3) What is the origin of the relatively high Th/Sm and REE abundances? Although modeling the meteorite petrogenesis in detail is necessarily limited because it is a single sample rather than part of a collected suite, low-Ti basalts from Apollo 12 and 15 can be used to provide some context for examining geochemical evolution of NWA 032.

Acknowledgements–This work was supported by NASA grants NAG 5-4212 (K. Keil, P. I.), NAG5-4172 (L. Haskin, P. I.), NAG5-8609 (R. Korotev, P. I.), and RTOP 344-38-12-02 (T. Bunch, P. I.); NSF grant EAR 9815338 (R. N. Clayton, P. I.); the Swiss National Science Foundation; and the European Commission *via* a Marie Curie Research Fellowship awarded to V. A. Fernandes. We thank Walt Radonsky for generously providing some of the sample material used in this study. We appreciate the technical assistance of Clifford Todd with the electron microprobe, and discussions with Yucheng Pan, E. R. D. Scott, and T. Hicks. We thank H. E. Jenin and A. Chaoui for technical assistance in the noble gas mass spectrometry. The manuscript was improved by reviews of L. A. Taylor and C. K. Shearer. This is Hawai'i Institute of Geophysics and Planetology publication no. 1183 and School of Ocean and Earth Sciences and Technology publication no. 5875.

Editorial handling: P. H. Warren

REFERENCES

ARMIENTI P., PARESCHI M. T., INNOCENTI F. AND POMPILIO M. (1994) Effects of magma storage and ascent on the kinetics of crystal growth. *Contrib. Mineral. Petrol.* **115**, 402–414.

ASIMOW P. D. AND GHIORSO M. S. (1998) Algorithmic modifications extending MELTS to calculate subsolidus phase relations. *Am. Mineral.* **83**, 1127–1132.

BENCE A. E. AND PAPIKE J. J. (1972) Pyroxenes as recorders of lunar basalt petrogenesis: Chemical trends due to crystal-liquid interaction. *Proc. Lunar Sci. Conf.* **3rd**, 431–469.

BENCE A. E., PAPIKE J. J. AND PREWITT C. T. (1970) Apollo 12 clinopyroxenes: Chemical trends. *Earth Planet. Sci. Lett.* **8**, 393–399.

BISCHOFF A. *ET AL.* (1998) Petrology, chemistry, and isotopic compositions of the lunar highland regolith breccia Dar al Gani 262. *Meteorit. Planet. Sci.* **33**, 1243–1257.

BURGESS R. AND TURNER G. (1998) Laser argon-40–argon-39 age determinations of Luna 24 mare basalts. *Meteorit. Planet. Sci.* **33**, 921–935.

BUSCHE F. D., PRINZ M., KEIL K. AND BUNCH T. E. (1972) Spinels and the petrogenesis of some Apollo 12 igneous rocks. *Am. Mineral.* **57**, 1729–1747.

CASHMAN K. V. (1993) Relationship between plagioclase crystallization and cooling rate in basaltic melts. *Contrib. Mineral. Petrol.* **113**, 126–142.

CASHMAN K. V. AND MARSH B. D. (1988) Crystal size distribution (CSD) in rocks and the kinetics and dynamics of crystallization, II: Makaopuhi lava lake. *Contrib. Mineral. Petrol.* **99**, 292–305.

CHAKRABORTY S. (1997) Rates and mechanisms of Mg-Fe interdiffusion in olivine at 980 °C–1300 °C. *J. Geophys. Res.* **102**, 12 317–12 331.

CHAO E. C. T. *ET AL.* (1970) Pyroxferroite, a new calcium-bearing iron silicate from Tranquillity Base. *Proc. Apollo 11 Lunar Sci. Conf.* **1st**, 65–79.

CHEN M., SHARP T. G., EL GORESY A., WOPENKA B. AND XIE X. (1996) The majorite-pyrope + magnesiowüstite assemblage: Constraints on the history of shock veins in chondrites. *Science* **271**, 1570–1573.

CLAYTON R. N. AND MAYEDA T. K. (1963) The use of bromine pentafluoride in the extraction of oxygen from oxides and silicates for isotopic analysis. *Geochim. Cosmochim. Acta* **27**, 43–52.

CLAYTON R. N. AND MAYEDA T. K. (1983) Oxygen isotopes in eucrites, shergottites, nakhlites, and chassignites. *Earth Planet. Sci. Lett.* **62**, 1–6.

COX K. G., BELL J. D. AND PANKHURST R. J. (1979) *The Interpretation of Igneous Rocks.* Unwin Hyman, London, U.K. 450 pp.

CRAWFORD M. L. (1973) Crystallization of plagioclase in mare basalts. *Proc. Lunar Sci. Conf.* **4th**, 705–717.

CRISP J., CASHMAN K. V., BONINI J. A., HOUGEN S. A. AND PIERI D. C. (1994) Crystallization history of the 1984 Mauna Loa lava flow. *J. Geophys. Res.* **99**, 7177–7198.

DICKINSON T., TAYLOR G. J., KEIL K., SCHMITT R. A., HUGHES S. S. AND SMITH M. R. (1985) Apollo 14 aluminous Mare basalts and their possible relationship to KREEP. *Proc. Lunar Planet. Sci. Conf.* **15th**, C365–C374.

DONALDSON C. H. (1976) An experimental investigation of olivine morphology. *Contrib. Mineral. Petrol.* **57**, 187–213.

EL GORESY A. AND RAMDOHR P. (1975) Subsolidus reduction of lunar opaque oxides: Textures, assemblages, geochemistry, and evidence for a late-stage endogenic gaseous mixture. *Proc. Lunar Sci. Conf.* **6th**, 729–745.

EL GORESY A., RAMDOHR P. AND TAYLOR L. A. (1971) The opaque minerals in the lunar rocks from Oceanus Procellarum. *Proc. Lunar Sci. Conf.* **2nd**, 219–235.

EL GORESY A., PRINZ M. AND RAMDOHR P. (1976) Zoning in spinels as an indicator of the crystallization histories of mare basalts. *Proc. Lunar Sci. Conf.* **7th**, 1261–1279.

EUGSTER O. AND MICHEL T. (1995) Common asteroid break-up events of eucrites, diogenites and howardites and cosmic-ray exposure production rates for noble gases in achondrites. *Geochim. Cosmochim. Acta* **59**, 177–199.

EUGSTER O., MICHEL T., NIEDERMANN S., WANG D. AND YI W. (1993) The record of cosmogenic, radiogenic, fissiogenic, and trapped noble gases in recently recovered Chinese and other chondrites. *Geochim. Cosmochim. Acta* **57**, 1115–1142.

FERNANDES V. A., BURGESS R. AND TURNER G. (2000) Laser argon-40–argon-39 studies of Dar al Gani 262 lunar meteorite. *Meteorit. Planet. Sci.* **35**, 1355–1364.

FERNANDES V. A., BURGESS R. AND TURNER G. (2001) Northwest Africa 032 (NWA 032): Evidence for lunar volcanism at 2.80 Ga (abstract). *Meteorit. Planet. Sci.* **36** (**Suppl.**), A57.

GHIORSO M. S., HIRSCHMANN M. AND SACK R. O. (1994) MELTS: Software for thermodynamic modeling of magmatic systems (abstract). *EOS Trans. Am. Geophys. Union* **75**, 571.

HIESINGER H., JAUMANN R., NEUKUM G. AND HEAD J. W. I. (2000) Ages of mare basalts on the lunar nearside. *J. Geophys. Res.* **105**, 29 239–29 275.

JAROSEWICH E. (1990) Chemical analyses of meteorites: A compilation of stony and iron meteorite analyses. *Meteoritics* **25**, 323–337.

JOLLIFF B. L., GILLIS J. J., HASKIN L. A., KOROTEV R. L. AND WIECZOREK M. A. (2000) Major lunar crustal terranes: Surface expressions and crust-mantle origins. *J. Geophys. Res.* **105**, 4197–4216.

KALLEMEYN G. W. AND WARREN P. H. (1983) Compositional implications regarding the lunar origin of the meteorite ALHA81005. *Geophys. Res. Lett.* **10**, 833–836.

KIRKPATRICK R. J. (1975) Crystal growth from a melt—A review. *Am. Mineral.* **60**, 798–814.

KIRKPATRICK R. J. (1977) Nucleation and growth of plagioclase, Makaopuhi and Alae lava lakes, Kilauea Volcano, Hawaii. *Geol. Soc. Am. Bull.* **88**, 78–84.

KOEBERL C., KURAT G. AND BRANDSTÄTTER F. (1993) Gabbroic lunar mare meteorites Asuka-881757 (Asuka-31) and Yamato-793169: Geochemical and mieralogical study. *Proc. NIPR Symp. Antarct. Meteorites* **6**, 14–34.

KOROTEV R. L. (1991) Geochemical stratigraphy of two regolith cores from the central highlands of the Moon. *Proc. Lunar Planet. Sci. Conf.* **21st**, 229–289.

KOROTEV R. L. (1996) On the relationship between the Apollo 16 ancient regolith breccias and feldspathic fragmental breccias, and the composition of the prebasin crust in the Central Highlands of the Moon. *Meteorit. Planet. Sci.* **31**, 403–412.

KOROTEV R. L. (2000) The great lunar hot spot and the composition and origin of the Apollo mafic ("LKFM") impact-melt breccias. *J. Geophys. Res.* **105**, 4317–4345.

KOROTEV R. L., JOLLIFF B. L., WANG A., GILLIS J. J., HASKIN L. A., FAGAN T. J., TAYLOR G. J. AND KEIL K. (2001) Trace-element concentrations in Northwest Africa 032 (abstract). *Lunar Planet. Sci.* **32**, #1451, Lunar and Planetary Institute, Houston, Texas, USA (CD-ROM).

LAWRENCE D. H., FELDMAN W. C., BARRACLOUGH B. L., BINDER A. B., ELPHIC R. C., MAURICE S., MILLER M. C. AND PRETTYMAN T. H. (2000) Thorium abundances on the lunar surface. *J. Geophys. Res.* **105**, 20 307–20 331.

LOFGREN G. E. (1983) Effect of heterogeneous nucleation on basaltic textures: A dynamic crystallization study. *J. Petrol.* **24**, 229–255.

LOFGREN G., DONALDSON C. H., WILLIAMS R. J., MULLINS O. J. AND USSELMAN T. M. (1974) Experimentally reproduced textures and mineral chemistry of Apollo 15 quartz normative basalts. *Proc. Lunar Sci. Conf.* **5th**, 549–567.

LONGHI J., WALKER D. AND HAYS J. F. (1976) Fe and Mg in plagioclase. *Proc. Lunar Sci. Conf.* **7th**, 1281–1300.

LUCEY P. G., BLEWETT D. T. AND JOLLIFF B. L. (2000) Lunar iron and titanium abundance algorithms based on final processing of Clementine ultraviolet-visible images. *J. Geophys. Res.* **105**, 20 297–20 305.

MARVIN U. B. (1983) The discovery and initial characterization of Allan Hills 81005: The first lunar meteorite. *Geophys. Res. Lett.* **10**, 775–778.

MCCONVILLE P., KELLEY S. AND TURNER G. (1988) Laser probe ^{40}Ar-^{39}Ar studies of the Peace River shocked L6 chondrite. *Geochim. Cosmochim. Acta* **52**, 2487–2499.

MORGAN G. B., IV AND LONDON D. (1996) Optimizing the electron microprobe analysis of hydrous alkali aluminosilicate glasses. *Am. Mineral.* **81**, 1176–1185.

NEAL C. R. AND TAYLOR L. A. (1992) Petrogenesis of mare basalts: A record of lunar volcanism. *Geochim. Cosmochim. Acta* **56**, 2177–2211.

NEAL C. R., HACKER M. D., SNYDER G. A., TAYLOR L. A., LIU Y-G. AND SCHMITT R. A. (1994a) Basalt generation at the Apollo 12 site, part 1: New data, classification, and re-evaluation. *Meteoritics* **29**, 334–348.

NEAL C. R., HACKER M. D., SNYDER G. A., TAYLOR L. A., LIU Y-G. AND SCHMITT R. A. (1994b) Basalt generation at the Apollo 12 site, Part 2: Source heterogeneity, multiple melts, and crustal contamination. *Meteoritics* **29**, 349–361.

NISHIIZUMI K. AND CAFFEE M. W. (2001) Exposure histories of lunar meteorites Northwest Africa 032 and Dhofar 081 (abstract). *Lunar Planet. Sci.* **32**, #2101, Lunar and Planetary Institute, Houston, Texas, USA (CD-ROM).

ONORATO P. I. K., UHLMANN D. R., TAYLOR L. A., COISH R. A. AND GAMBLE R. P. (1978) Olivine cooling speedometers. *Proc. Lunar Sci. Conf.* **9th**, 613–628.

PAPIKE J. J. (1998) Comparative planetary mineralogy: Chemistry of melt-derived pyroxene, feldspar, and olivine. In *Planetary Materials* (ed. J. J. Papike), pp. 7-1 to 7-11. Reviews in Mineral. **36**, Mineralogical Society of America, Washington, D.C., USA.

PAPIKE J. J., HODGES F. N., BENCE A. E., CAMERON M. AND RHODES J. M. (1976) Mare basalts: Crystal chemistry, mineralogy, and petrology. *Rev. Geophys. Space Phys.* **14**, 475–540.

PAPIKE J. J., RYDER G. AND SHEARER C. K. (1998) Lunar samples. In *Planetary Materials* (ed. J. J. Papike), pp. 5-1 to 5-234. Reviews in Mineralogy **36**, Mineralogical Society of America, Washington, D.C., USA.

RHODES J. M. AND HUBBARD N. J. (1973) Chemistry, classification, and petrogenesis of Apollo 15 mare basalts. *Proc. Lunar Sci. Conf.* **4th**, 1127–1148.

RHODES J. M., BLANCHARD D. P., DUNGAN M. A., BRANNON J. C. AND RODGERS K. V. (1977) Chemistry of Apollo 12 mare basalts: Magma types and fractionation processes. *Proc. Lunar Sci. Conf.* **8th**, 1305–1338.

ROEDER P. L. AND EMSLIE R. F. (1970) Olivine-liquid equilibrium. *Contrib. Mineral. Petrol.* **29**, 275–289.

RYDER G. AND SCHURAYTZ B. C. (2001) Chemical variation of the large Apollo 15 olivine-normative mare basalt rock samples. *J. Geophys. Res.* **106**, 1435–1451.

SCHAAL R. B. AND HÖRZ F. (1977) Shock metamorphism of lunar and terrestrial basalts. *Proc. Lunar Sci. Conf.* **8th**, 1697–1729.

SCHMITT H. H. (1991) Evolution of the Moon: Apollo model. *Am. Mineral.* **76**, 773–784.

SNYDER G. A. AND TAYLOR L. A. (2001) Oldest mare basalts or impact melts? The role of differential melting of plagioclase in Apollo 14 high-Al basalts (abstract). *Meteorit. Planet. Sci.* **36 (Suppl.)**, A194.

STÖFFLER D., BISCHOFF A., BUCHWALD V. AND RUBIN A. E. (1988) Shock effects in meteorites. In *Meteorites and the Early Solar System* (eds. J. F. Kerridge and M. S. Matthews), pp. 165–202. Univ. Arizona Press, Tucson, Arizona, USA.

TAKEDA H., ARAI T. AND SAIKI K. (1993) Mineralogical studies of lunar meteorite Yamato-793169. *Proc. NIPR Symp. Antarct. Meteorites* **6**, 3–13.

TAYLOR L. A., NAZAROV M. A., COHEN B. A., WARREN P. H., BARSUKOVA L. D., CLAYTON R. N. AND MAYEDA T. K. (2001) Bulk chemistry and oxygen isotopic compositions of lunar meteorites Dhofar 025 and Dhofar 026: A second-generation impact melt (abstract). *Lunar Planet. Sci.* **32**, #1985, Lunar and Planetary Institute, Houston, Texas, USA (CD-ROM).

THALMANN C., EUGSTER O., HERZOG G. F., KLEIN J., KRÄHENBÜHL U., VOGT S. AND XUE S. (1996) History of lunar meteorites Queen Alexandra Range 93069, Asuka-881757, and Yamato-793169 based on noble gas isotopic abundances, radionuclide concentrations, and chemical composition. *Meteorit. Planet. Sci.* **31**, 857–868.

THOMPSON J. B., JR. (1982) Composition space: An algebraic and geometric approach. In *Characterization of Metamorphism Through Mineral Equilibria* (ed. J. M. Ferry), pp. 1–31. Reviews in Mineralogy **10**, Mineralogical Society of America, Washington, D.C., USA.

THOMPSON J. B., JR. (1991) Modal space: Applications to ultramafic and mafic rocks. *Can. Mineral.* **29**, 615–632.

TURNER G. AND CADOGAN P. H. (1974) Possible effects of ^{39}Ar recoil in ^{40}Ar-^{39}Ar dating. *Proc. Lunar Sci. Conf.* **5th**, 1601–1615.

TURNER G., HUNEKE J. C., PODOSEK F. A. AND WASSERBURG G. J. (1971) ^{40}Ar-^{39}Ar ages and cosmic ray exposure ages of Apollo 14 samples. *Earth Planet. Sci. Lett.* **12**, 19–35.

VOGT S. *ET AL.* (1993) Exposure history of the lunar meteorite, Elephant Moraine 87521. *Geochim. Cosmochim. Acta* **57**, 3793–3799.

WARREN P. H. AND KALLEMEYN G. W. (1989) Elephant Moraine 87521: The first lunar meteorite composed of predominantly mare material. *Geochim. Cosmochim. Acta* **53**, 3323–3300.

WARREN P. H. AND KALLEMEYN G. W. (1991a) Geochemical investigation of five lunar meteorites: Implications for the composition, origin and evolution of the lunar crust. *Proc. NIPR Symp. Antarct. Meteorites* **4**, 91–117.

WARREN P. H. AND KALLEMEYN G. W. (1991b) The MacAlpine Hills lunar meteorite, and implications of the lunar meteorites collectively for the composition and origin of the Moon. *Geochim. Cosmochim. Acta* **55**, 3123–3138.

WARREN P. H. AND KALLEMEYN G. W. (1993) Geochemical investigation of two lunar mare meteorites: Yamato-793169 and Asuka-881757. *Proc. NIPR Symp. Antarct. Meteorites* **6**, 35–57.

WARREN P. H., TAYLOR L. A., KALLEMEYN G., COHEN B. A. AND NAZAROV M. A. (2001) Bulk-compositional study of three lunar meteorites: Enigmatic siderophile element results for Dhofar 026 (abstract). *Lunar Planet. Sci.* **32**, #2197, Lunar and Planetary Institute, Houston, Texas, USA (CD-ROM).

WENK H. R. AND WILDE W. R. (1973) Chemical anomalies of lunar plagioclase, described by substitution vectors and their relation to optical and structural properties. *Contrib. Mineral. Petrol.* **41**, 89–104.

WLOTZKA F. (1993) A weathering scale for the ordinary chondrites (abstract). *Meteoritics* **28**, 460.

YANAI K. AND KOJIMA H. (1991) Varieties of lunar meteorites recovered from Antarctica. *Proc. NIPR Symp. Antarct. Meteorites* **4**, 70–90.

APPENDIX

Table A1 appears on the next page.

TABLE A1. Ar-Ar stepped heating data for G3 and G4 samples of NWA 032 lunar meteorite (1σ errors).

Temp. (°C)	^{36}Ar ($\times 10^{-11}$ cm^3)	^{37}Ar	^{38}Ar	^{39}Ar	^{40}Ar	K (ppm)	Ca (wt%)	Exposure age (Ma)*	Age (Ga)
G3 sample wt = 0.014073 g		**J = 0.01260 ± 0.000126; α = 0.4812 ± 0.0001; β = 6.95 ± 0.03**							
200	0.10 ± 0.02	1.23 ± 0.06	0.52 ± 0.02	0.29 ± 0.15	58.99 ± 0.08	2.4 ± 1.2	0.002 ± 0.001	1598 ± 262	2.281 ± 0.648
400	1.05 ± 0.02	19.43 ± 0.12	3.01 ± 0.03	8.59 ± 0.10	2842.11 ± 1.26	70.5 ± 1.1	0.032 ± 0.001	599.3 ± 23.8	2.963 ± 0.018
500	5.40 ± 0.01	32.56 ± 0.18	3.39 ± 0.03	11.89 ± 0.08	5658.48 ± 3.70	97.6 ± 1.2	0.054 ± 0.001	501.1 ± 19.0	3.509 ± 0.011
550	1.67 ± 0.01	32.73 ± 0.16	3.16 ± 0.02	9.05 ± 0.07	3217.15 ± 1.90	74.3 ± 0.9	0.055 ± 0.001	386.1 ± 11.7	3.068 ± 0.011
600	2.69 ± 0.01	55.00 ± 0.05	4.34 ± 0.03	10.85 ± 0.03	3494.97 ± 1.71	89.0 ± 0.9	0.092 ± 0.001	321.1 ± 8.7	2.925 ± 0.004
650	4.04 ± 0.03	93.29 ± 0.06	6.46 ± 0.02	12.52 ± 0.05	3541.36 ± 1.58	102.8 ± 1.1	0.156 ± 0.002	282.1 ± 4.7	2.738 ± 0.006
700	5.80 ± 0.03	148.35 ± 0.09	9.34 ± 0.03	12.47 ± 0.05	3398.30 ± 1.09	102.3 ± 1.1	0.248 ± 0.002	256.4 ± 4.0	2.687 ± 0.010
750	8.81 ± 0.02	237.84 ± 0.10	13.88 ± 0.05	12.07 ± 0.08	3319.88 ± 0.95	99.1 ± 1.2	0.398 ± 0.004	238.3 ± 3.4	2.699 ± 0.010
800	14.90 ± 0.02	435.60 ± 0.22	23.88 ± 0.03	12.47 ± 0.06	3329.82 ± 2.33	102.3 ± 1.1	0.728 ± 0.007	223.3 ± 2.4	2.659 ± 0.006
850	10.78 ± 0.01	309.06 ± 0.73	17.20 ± 0.02	8.78 ± 0.05	1883.11 ± 0.67	72.1 ± 0.8	0.517 ± 0.005	226.9 ± 2.6	2.361 ± 0.008
900	7.91 ± 0.02	225.33 ± 0.41	12.44 ± 0.02	4.93 ± 0.04	981.21 ± 0.28	40.4 ± 0.5	0.377 ± 0.004	225.5 ± 2.7	2.265 ± 0.011
1000	43.96 ± 0.01	1127.82 ± 1.65	62.81 ± 0.02	16.66 ± 0.10	5165.42 ± 3.24	136.7 ± 1.6	1.885 ± 0.019	228.0 ± 2.3	2.870 ± 0.009
1050	89.66 ± 0.04	2659.95 ± 2.38	141.81 ± 0.05	23.97 ± 0.05	5085.12 ± 2.40	196.8 ± 2.0	4.446 ± 0.045	218.3 ± 2.2	2.347 ± 0.003
1100	7.41 ± 0.02	215.93 ± 1.81	11.33 ± 0.02	1.22 ± 0.04	262.47 ± 0.11	10.0 ± 0.4	0.361 ± 0.005	214.8 ± 3.3	2.365 ± 0.047
1200	10.53 ± 0.02	310.96 ± 1.13	16.74 ± 0.02	1.19 ± 0.07	254.16 ± 0.19	9.8 ± 0.6	0.520 ± 0.006	220.4 ± 2.6	2.356 ± 0.076
1400	0.86 ± 0.03	14.74 ± 0.07	0.77 ± 0.02	0.06 ± 0.04	110.13 ± 0.08	0.5 ± 0.4	0.025 ± 0.001	213.5 ± 26.8	5.780 ± 1.294
1600	0.25 ± 0.02	0.57 ± 0.15	0.02 ± 0.02	0.05 ± 0.03	81.09 ± 0.13	0.4 ± 0.2	0.001 ± 0.001	n.d.	5.494 ± 1.024
Total	215.82 ± 0.09	5920.39 ± 3.72	331.12 ± 0.11	147.07 ± 0.30	42683.76 ± 6.98	1206.9 ± 4.4	9.895 ± 0.050	–	2.775 ± 0.067
G4 sample wt = 0.011730 g									
300	0.62 ± 0.01	6.62 ± 0.13	1.17 ± 0.04	2.55 ± 0.02	526.17 ± 0.15	25.1 ± 0.3	0.013 ± 0.001	708.1 ± 78.7	2.312 ± 0.011
400	0.86 ± 0.02	12.16 ± 0.08	1.13 ± 0.05	5.94 ± 0.02	2115.55 ± 0.61	58.4 ± 0.6	0.024 ± 0.001	388.1 ± 31.9	3.072 ± 0.005
450	0.94 ± 0.02	32.56 ± 0.10	1.23 ± 0.02	5.27 ± 0.05	2164.73 ± 0.79	51.9 ± 0.7	0.065 ± 0.001	157.9 ± 7.6	3.284 ± 0.014
500	0.96 ± 0.02	53.06 ± 0.05	1.69 ± 0.02	5.76 ± 0.03	2189.70 ± 0.65	56.7 ± 0.6	0.106 ± 0.001	128.1 ± 4.7	3.168 ± 0.007
600	2.87 ± 0.03	58.78 ± 0.10	4.27 ± 0.03	10.97 ± 0.04	3685.90 ± 1.26	108.0 ± 1.1	0.118 ± 0.001	298.7 ± 5.3	2.986 ± 0.005
650	3.55 ± 0.02	67.28 ± 0.14	4.66 ± 0.01	9.40 ± 0.04	2850.63 ± 0.84	92.6 ± 1.0	0.135 ± 0.001	289.5 ± 3.6	2.837 ± 0.007
700	5.63 ± 0.01	108.11 ± 0.14	6.93 ± 0.15	9.11 ± 0.05	2880.00 ± 1.03	89.7 ± 1.0	0.216 ± 0.002	270.5 ± 6.6	2.898 ± 0.007
750	7.34 ± 0.02	190.19 ± 0.15	11.31 ± 0.02	9.28 ± 0.05	2652.22 ± 0.91	91.4 ± 1.0	0.381 ± 0.004	243.4 ± 2.0	2.753 ± 0.008
800	12.29 ± 0.03	333.79 ± 0.09	18.32 ± 0.02	9.30 ± 0.03	2732.48 ± 0.82	91.6 ± 1.0	0.668 ± 0.007	225.6 ± 1.6	2.792 ± 0.004
850	9.75 ± 0.04	245.83 ± 0.20	13.92 ± 0.01	6.68 ± 0.04	1798.49 ± 0.52	65.8 ± 0.7	0.492 ± 0.005	234.0 ± 1.7	2.669 ± 0.007
900	8.97 ± 0.03	214.64 ± 0.11	11.88 ± 0.01	4.48 ± 0.03	1327.87 ± 0.45	44.1 ± 0.5	0.430 ± 0.004	231.1 ± 1.8	2.806 ± 0.010
1000	31.36 ± 0.04	895.72 ± 0.27	49.54 ± 0.04	11.10 ± 0.03	2285.88 ± 0.79	109.3 ± 1.1	1.793 ± 0.018	226.4 ± 1.5	2.308 ± 0.004
1050	55.96 ± 0.05	1625.06 ± 0.47	87.82 ± 0.04	13.22 ± 0.02	3015.47 ± 1.19	130.2 ± 1.3	3.252 ± 0.033	221.2 ± 1.4	2.443 ± 0.003
1100	13.78 ± 0.01	385.53 ± 0.20	20.79 ± 0.01	2.70 ± 0.03	767.92 ± 0.27	26.6 ± 0.4	0.772 ± 0.008	220.8 ± 1.5	2.745 ± 0.017
1400	10.75 ± 0.02	288.35 ± 0.17	15.85 ± 0.01	1.87 ± 0.02	613.96 ± 0.25	18.4 ± 0.3	0.577 ± 0.006	225.0 ± 1.6	2.949 ± 0.016
1600	0.57 ± 0.01	0.79 ± 0.13	0.21 ± 0.02	0.09 ± 0.02	218.97 ± 0.21	0.9 ± 0.2	0.002 ± 0.001	1065 ± 524	6.190 ± 0.317
Total	166.21 ± 0.10	4518.48 ± 0.74	250.72 ± 0.19	107.73 ± 0.14	31825.94 ± 3.00	1060.7 ± 3.3	9.042 ± 0.040	–	2.800 ± 0.014

*Exposure age based on $^{38}Ar_c$/Ca production rate of 9.05×10^{-9} cm^3 g^{-1} Ca Ma^{-1} (Eugster and Michel, 1995). Errors are analytical precision and do not account for uncertainties in the production rate. n.d. = not detected.